공학박사학위논문

레이저 분광 기술을 활용한 실시간 비접촉 탐사용 성분 분석 기법 연구

A study on the component analysis method using laser spectroscopy for the real time stand-off space exploration

2015년 2월

서울대학교 대학원

기계항공공학부

최 수 진

Abstract

A study on the component analysis method using laser spectroscopy for the real time stand-off space exploration

Soo-Jin Choi
Mechanical and Aerospace Engineering
The Graduate School
Seoul National University

The Laser-Induced Breakdown Spectroscopy (LIBS) has great advantages as an analytical technique, namely real-time rapid analysis without sample preparation and stand-off detection capability, ideal for mobile chemical sensor for space exploration. In this research, we investigated the LIBS specification required to build the payload for space exploration and prepared the basis for real circumstances analysis by building a vacuum chamber for space environment. We also built a database to understand the effect of LIBS signals with respect to the properties of laser and samples and to predict the plasma signal under the working circumstances that changed through the application of low pressure condition. Moreover, we built a database of quantitative analysis by drawing the calibration curves with the effects of pressure, elements and samples utilizing the certified reference materials

(CRMs) which are appropriate for the space exploration and investigated the characteristics of the samples. Researches of stand-off detection were carried out for further understanding of space science by considering the environmental condition. The confinement method was devised to enhance the signal for optimum plasma detection at space environment. The results obtained through this research will allow more precise mapping compared to widely used conventional elemental analyzing method in space exploration and provide a guideline for design of various LIBS experiments.

***Keywords*: Laser-Induced Breakdown Spectroscopy (LIBS), Plasma, Laser ablation, Space exploration, Low pressure, Component analysis**

***Student Number*: 2008-20799**

LIST

LIST OF FIGURES

LIST OF TABLES

Preface

This thesis is based on the following publications and manuscripts.

Chapter 3
S.J. Choi, J. J. Yoh, "Effective LIBS detection using double pulse at optimum configuration," Applied Spectroscopy, Vol. 65, Issue 8, pp. 952-956, 2011.

Chapter 4
S.J. Choi, K.J. Lee, J.J. Yoh, "Quantitative laser-induced breakdown spectroscopy of standard reference materials of various categories," Applied Physics B, Vol. 113, Issue 3, pp 379-388, 2013.

Chapter 5
S.J. Choi, J.J. Yoh, "Laser-induced plasma peculiarity at low pressures from the elemental lifetime perspective," Optics Express, Vol 19, 23, pp. 23097-23103, 2011.

Chapter 6
K.J. Lee, S.J. Choi, J.J. Yoh, "Stand-off laser-induced breakdown spectroscopy of aluminum and geochemical reference materials at pressure below 1 torr," Spectrochimica Acta Part B, Vol. 101, pp. 335-341, 2014.

Chapter 7
S.J. Choi, K.J. Lee, J.J. Yoh, "The laser-induced plasma persistence time extension in low pressures using the ablated mass confinement method," Spectrochimica Acta Part B, Vol. 97, Issue 1, pp 113-117, 2014.

S.J. Choi, J.J. Choi, J.J. Yoh, "Novel control of plasma expansion direction aimed at very low pressure laser-induced plasma spectroscopy," Optics Express, in press, 2015.

The chapters are reproduced with permission of the co-authors and the publishers.

CHAPTER 1

INTRODUCTION

1.1 Motivation and purpose

The laser is already being widely used in micromachining, bioengineering and various measurement methods. Recently, there are number of researchers going on with a system that can integrates pulsed laser energy with space exploration technology such as laser propulsion that used the momentum generated by pulse laser energy, and laser-induced breakdown spectroscopy (LIBS) elemental analyzer that is using pulse laser energy as an exciting source.

In this work, component analysis by LIBS is utilized as a promising means of advancing space exploration. A space technology can be divided into 3 major areas – launch vehicle, satellite, and rover system. A LIBS system belongs to the rover payload (Fig. 1.1) to measure a composition of the surface and atmosphere and to obtain more precise mapping compared to conventional methods widely used. The purpose of this study is fundamental to understand the fundamental characteristics of the laser induced plasma and constructing of a database under the effects of various experimental parameters, different environmental conditions, and sample properties.

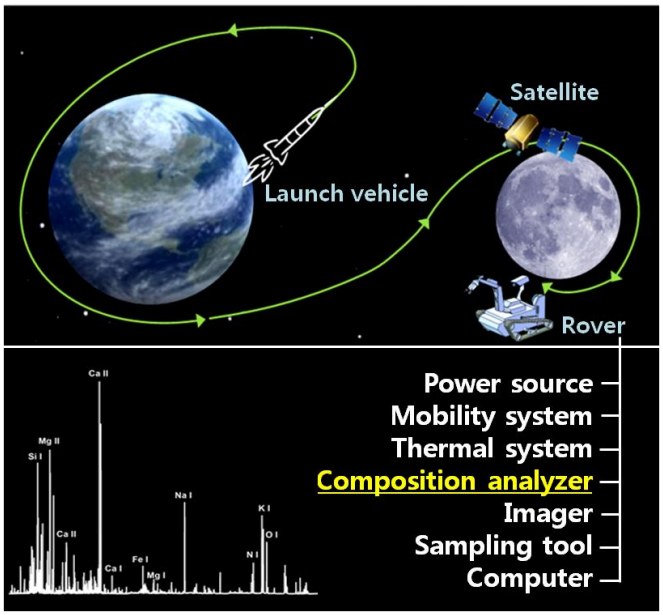

Fig. 1.1 The role of LIBS system

Currently, various spectroscopic tools well provide feasibility of identifying chemical elements of unknown resources on other planets. In particular, the gamma-ray spectrometer [1] and alpha-proton X-ray spectrometer [2] on board Mars probes have accomplished various space missions in the past. Table 1.1 shows the comparison of typical component analyzer for space exploration. A LIBS has low sensitivity to Cl, S, and F, but it can detect all elements with varying degrees of sensitivity. Especially it is more capable to detect the light elements unlike X-ray techniques, therefore LIBS can make up for the weak points in the current elemental analyzer.

Table 1.1 Comparison of typical payload for composition analysis

Payload	Ability	Disadvantage
X-ray spectroscopy (XRS)	- Mapping of surface composition	- Low sensitive to light elements
Gamma-ray spectroscopy (GRS)	- Mapping of surface composition - Can detect up to a depth of tens of cm to m	- Long acquisition time - Low resolution
Alpha particle X-ray spectroscopy (APXS)	- Micro PIXE can probe a very small spot on a sample (< 1 μm) - High sensitive to S, Cl, Br	- Low sensitive to light elements - Long acquisition time - In-situ (cm) detection
Neutron spectroscopy (NS)	- Detection of ice (< 0.01%) and ice beneath the surface up to 2 m	- Cosmic-ray produced neutrons give poor depth resolution - Limited to H detection
X-ray diffraction (XRD)	- Structure and composition of nearly all crystalline materials	- Typical analysis – 10 hours
Laser induced Breakdown spectroscopy (LIBS)	- Can detect all elements with varying degrees of sensitivity - Sensitive to the light elements (Unlike X-ray techniques) - Real time data acquisition	- Low sensitive to Cl, S, F

Table 1.2 indicates the comparison of mineralogy techniques. Phase or structural identification is possible using XRD and Raman spectroscopy. And many types of technique including LIBS can identify elemental composition. Some methods are capable to analyze microscopic scale and subsurface. We can develop the effective and complementary payload by combining LIBS with other spectroscopic methods. For example, analysis of elemental composition of surface/atmosphere and phase of minerals present and

morphology are possible using LIBS and phase/structural analyzer. Also combined LIBS system with GRS/XRS/APXS can detect most of elements rapidly with high sensitivity.

Table 1.2 Comparison of mineralogy techniques

Technique	Phase or structural identification	Elemental composition	Microscopic analysis	Subsurface penetration
GRS	X	○	X	○
NS	X	○ Limited to H	X	○
APXS	X	○	○	X
XRD	○	X	○ Potentially	X
XRF	X	○ > Na	○ Potentially	X
Raman	○	X	○	X
LIBS	X	○	○	○ ~10-100 μm

1.2 Laser-material interaction

A laser (Light Amplification by Stimulated Emission of Radiation) is a device that emits light which has characteristics of directivity, monochromatic, and coherence. The directivity is correlated with the divergence property of the laser beam which describes its angular spreading [3]. Laser beam propagates straightly while ordinary light source is emitting in all directions. The directivity describes qualitatively the property of the laser radiation to remain concentrated at long distance. The laser emits all photons with the same energy, and thus the same wavelength, it is said to be monochromatic. The light from a laser typically comes from one atomic transition with a single precise wavelength. So the laser light has a single spectral color and is almost the purest monochromatic light available. Also a laser differs from other sources of light because it emits light coherently. Spatial coherence allows a laser to be focused to a tight spot, enabling applications like laser cutting and lithography. Spatial coherence also allows a laser beam to stay narrow over long distances (collimation). Lasers can also have high temporal coherence which allows them to have a very narrow spectrum.

The laser-material interaction involves complex processes of heating, melting, vaporization, ejection of atoms, ions and molecules, shock waves, plasma initiation and plasma expansion. It is dependent on several variables such as pulse duration, irradiance, and so forth.

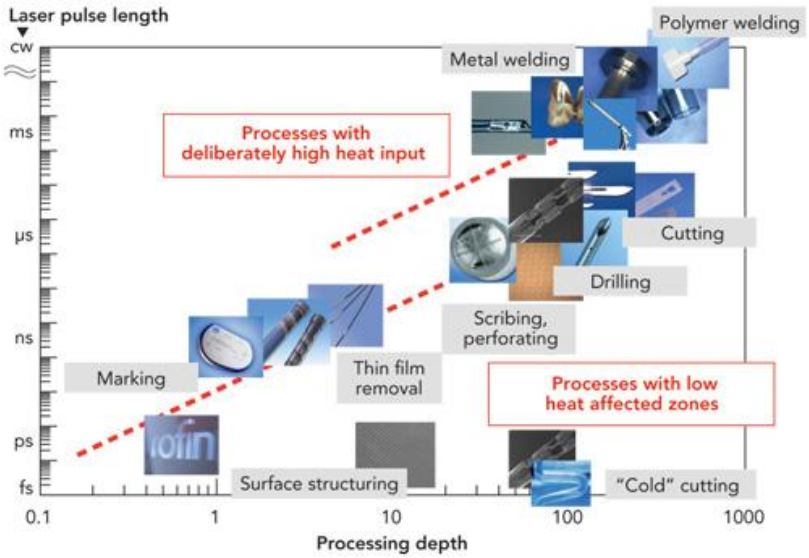

Fig. 1.2 Classification of laser applications in medical device manufacturing regarding with pulse duration [4]

Figure 1.2 shows the classification of laser application in medical device manufacturing regarding with pulse duration. Laser-material interaction can be divided into two major phenomena. In long pulse duration, the most energy of laser irradiation is transferred into heat due to absorption of the photons by samples while the generated electrons have low ionization potential. Meanwhile, short pulse duration causes laser ablation due to high irradiance ($> 10^9$ W/cm^2) of laser energy. At this high irradiance, temperature of the sample surface rises substantially above the vaporization temperature. Once plasma is generated by high irradiance of laser, plasma is expanded as a plume which drives a shock wave towards the incoming laser beam as shown

Fig. 1.3 [5]. The plasma and shockwave generated by laser ablation phenomena widely used in spectroscopic analysis, particle acceleration, laser propulsion, precision processing, and etc.

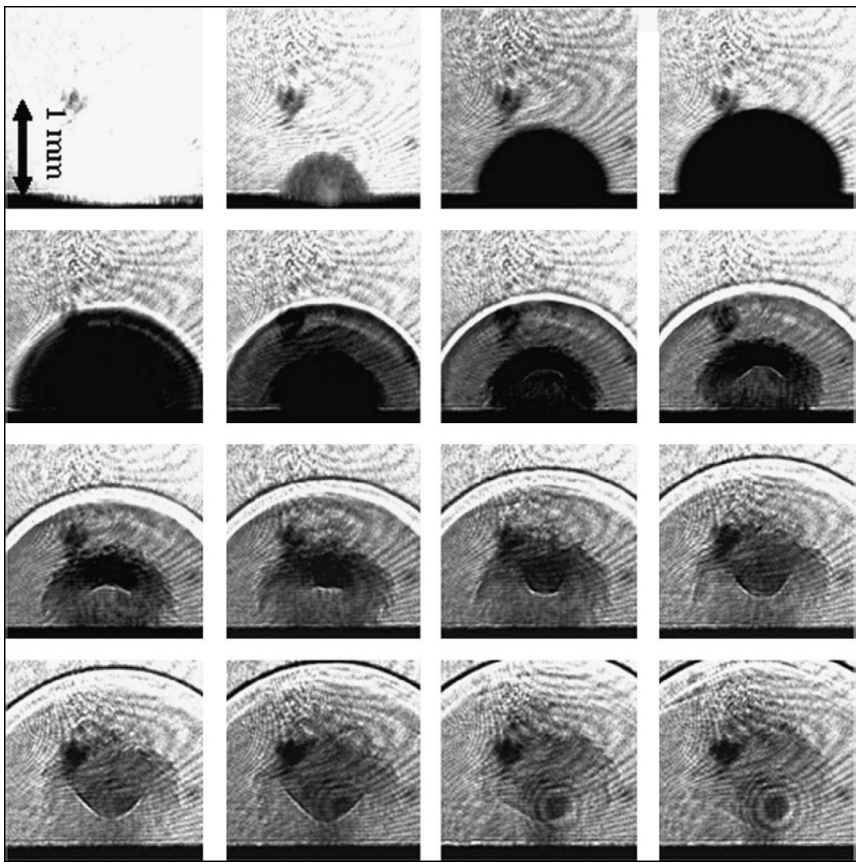

Fig. 1.3 A plasma and shockwave generation by 4 GW/cm^2 irradiance. The first image is recorded simultaneously with the operation of the ablation pulse, and the following images have a 20 ns time step [5]

At the early time after initiation of the plasma, extremely high temperature is sustained, thus the ablated material dissociates into excited ions and atoms. As the plasma cools, the plasma emits a strong “white light” continuum which has broad wavelength because of bremsstrahlung and radiation from recombination processing of free electrons and ions. The optimum delay time that is the time between laser irradiation and opening the shutter of a spectrometer is one of important parameters in LIBS, since, the plasma signal is dominated by continuum in the early time.

1.3 Laser-Induced Breakdown Spectroscopy (LIBS) for space exploration

LIBS is a type of atomic analyzer using the plasma generated by laser ablation. The emitted light from the plasma provides characteristic spectra for each element and by identifying the spectra, the chemical composition of each sample can be rapidly determined as shown in Fig. 1.4. LIBS has many advantages as space exploration tool such as real-time processing, stand-off detection, and no necessary sample preparation. Also all phases of material component analysis and depth profiling are possible. Such overwhelming advantages over the previous detection techniques have led researchers to become more aware of space resource exploration using LIBS technology.

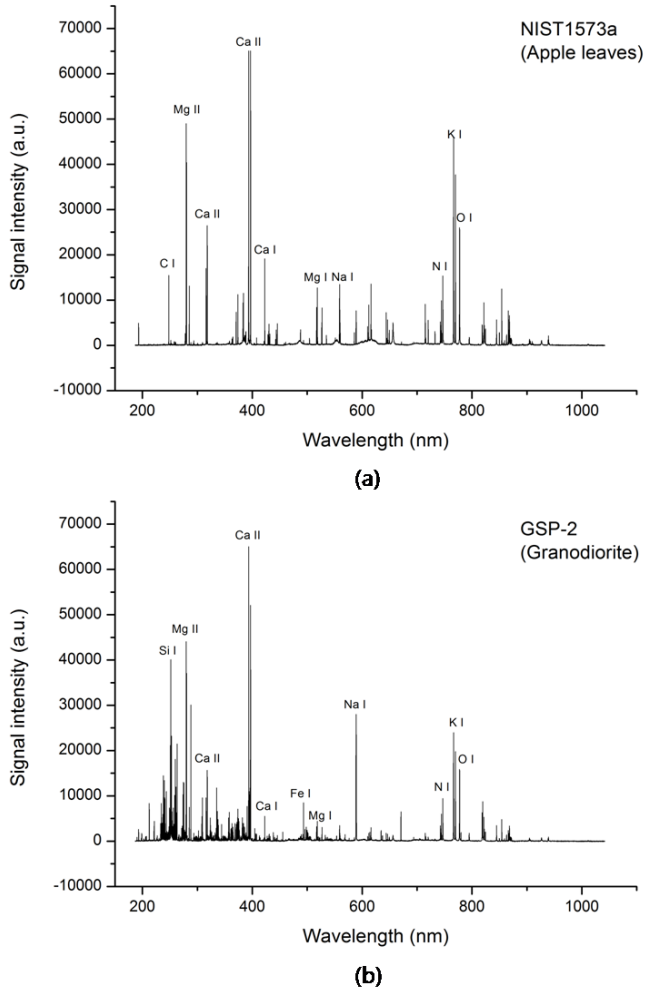

Fig. 1.4 LIBS spectra of certified reference materials

(a) NIST 1573a, (b) GSP-2

LIBS is used in industry, biomedical and forensic application, analysis of hazardous material such as explosive and nuclear materials, underwater analysis, nutrient analysis, and planetary exploration. For space missions, analysis of low pressure effect and stand-off detection should be performed as

well as comprehensive studies, including optimizing the experimental parameters, qualitative and quantitative analysis, etc. Colao et al. established the optimal experimental conditions for the signal acquisition in the multi-elemental LIBS quantitative analysis under the simulated planet atmosphere [6]. To perform quantitative analysis, chemometrics methods such as PLS, PCA, and SIMCA were employed to analyze remote LIBS spectra as a means of exploiting the chemical matrix effects [7,8]. Sallé et al. used geological samples at 5 m distance in 7 torr to simulate Martian atmosphere [9,10]. They conducted quantitative analysis of in-situ and stand-off conditions by calculating the calibration curves. Thompson et al. carried out quantitative analysis and classification of Martian meteorite samples at 5.4 m distance in 7 torr [11]. Cousin et al. tried pyroxene samples at 3 m distance inside a 7 torr chamber in order to build Martian database for the Mars mission [12].

Up to now, the first and only application of LIBS for space mission is ChemCam. The ChemCam have found out the key chemical ingredients for life are present, such as carbon, hydrogen, nitrogen, oxygen, phosphorus, and sulfur on Mars. Also ChemCam is possible to remove dust using three hundreds laser pulses and detects dust and target surface [13,14]. Dust tends to cover everything on Mars or lunar surface. ChemCam has the capability to remove this layer to access the underlying rock and expose dust-free surfaces to other optical investigations.

Figure 1.5 represents the overview of this study. The aim of this study is not

developing the whole components of LIBS, but focusing on the research technique through the optimized design of building a database and the acquisition of technology for the space exploration. Fundamental study was carried out to investigate characteristics the laser-induced plasma. LIBS specification required to build the payload for space exploration was identified based on the information of ChemCam and prepared the base of the research considering real management circumstances by building up a vacuum chamber which simulates a space environment up to 10^{-5} torr. Various databases were constructed to understand the effect of LIBS signals toward the properties of laser and samples and to predict the characteristics under the working circumstances that is changing through the application of low pressure condition. Database of quantitative analysis was built by univariate and multivariate analysis utilizing the certified reference materials (CRMs) which are appropriate for the space exploration. Moreover researches of stand-off detection were carried out to confirm the capability of LIBS system as a rover payload by considering the environmental condition. We built a compact LIBS prototype by combining commercial device such as laser, spectrometer, and telescope to qualify the performance of compact LIBS system as a stand-off analyzer at low pressure condition. A spatial confinement method was developed to control the direction of the expanding plasma for enhancement of electron density at low pressure condition by preventing a rapid plasma expansion.

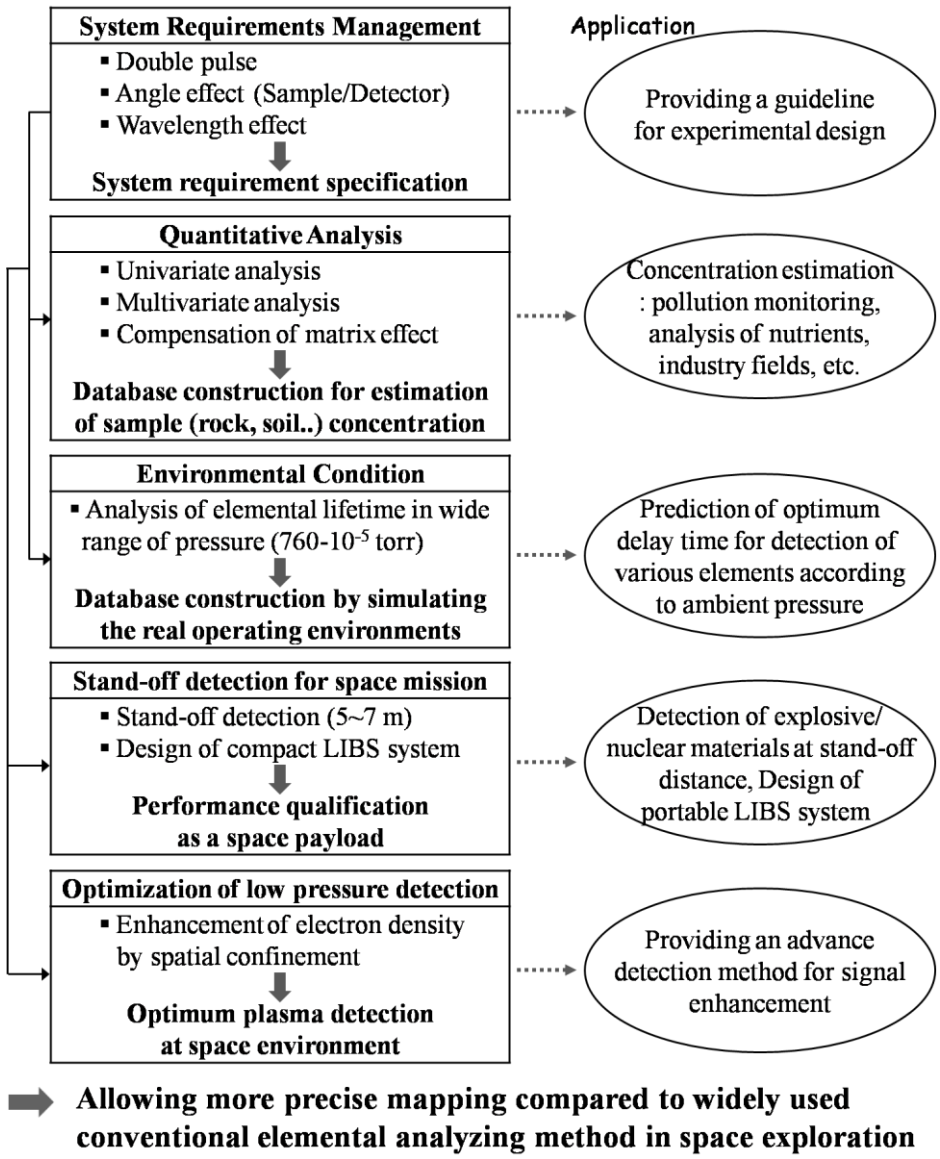

Fig. 1.5 Overview of this study

Especially, we made an effort to discover the elemental characteristics using physicochemical properties for effective detection. Optimal detecting condition and delay time of ions, atoms, and molecules of each element are strongly dependant on elemental characteristics. We observed plasma signals of various elements which have different properties with high temporal resolution to build database of optimum detecting condition.

The works reported here provide guidelines for designs of experimental setup appropriately for purpose of LIBS research.

CHAPTER 2

EXPERIMENTAL APPARATUS

LIBS system basically consists of laser for plasma generation, detector and spectrometer for plasma detection, and various optical components such as lens, mirror, beam expander, etc. as shown in Fig. 2.1. In this study, different devices were used to carry out various experiments considering the purpose of experiments. Considered variables of device were pulse duration, wavelength, pulse energy for laser and wavelength range, gate width for spectrometer.

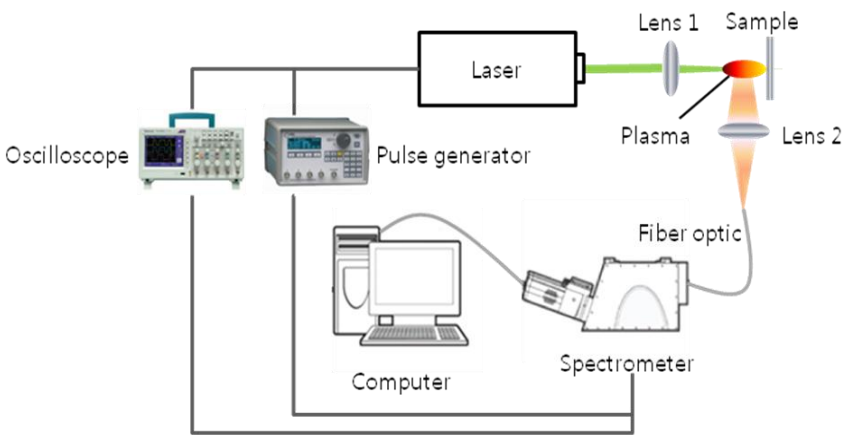

Fig. 2.1 Fundamental experimental apparatus of LIBS

2.1 Laser

In this experiment, three types of laser were used for different object.

A LIBS system (RT250-Ec, Applied Spectra Inc.) was used to carry out the experiment on quantitative analysis using univariate and multivariate method, signal enhancement by confinement method, and investigation of environment effect (Fig. 2.2). The RT250 Nd:YAG laser operating at 1064 nm with a maximum pulse energy of 110 mJ.

Surelite Nd:YAG laser (Continuum) used for fundamental study and stand-off detection, and investigation of environment effect (Fig. 2.3). Surelite laser emits four wavelengths at 1064, 532, 355, 266 nm using harmonic generator and dichroic mirror. Maximum energy at 1064 nm is 450 mJ at 10 Hz repetition rate.

Fig. 2.2 RT250-Ec Nd:YAG laser

Minilite Nd:YAG laser (Continuum) that can emit dual pulse using two power supplies (Fig. 2.4) was applied for double pulse experiment. The wavelength is 532 nm with 25 mJ maximum pulse energy thus when the two pulses are emitted simultaneously at a combined energy of 50 mJ.

Fig. 2.3 Surelite Nd:YAG laser

Fig. 2.4 Dual-pulse Minilite Nd:YAG laser

2.2 Spectrometer and detector

The emitted light from the plasma is collected by fiber optic cable with different core diameter. In this study, two spectrometers that are ICCD coupled echelle grating spectrometer and 6 channel CCD coupled spectrometer were used.

For fundamental study and stand-off detection, plasma is collimated on the entrance slit of the echelle grating spectrometer (Andor Mechelle), coupled to the gated ICCD (Andor, iStar), which allows the simultaneous spectral recording in the range 200 to 975 nm with a spectral resolution ($\lambda/\Delta\lambda$) of 5000 namely 0.1 nm resolution (Fig. 2.5).

High resolution 6 channel CCD spectrometer (Aurora, Applied Spectra Inc.) that covers the spectrum ranging from 190 to 1040 nm was also used for quantitative analysis and signal enhancement (Fig. 2.6). The spectral resolution of the spectrometer is less than 0.1 nm for UV to VIS and 0.12 nm for VIS to NIR range.

CCD detector has long gate width in the order of ms while an intensified CCD (ICCD) can enhance time resolution using an MCP intensifier (Micro-Channel Plate Image Intensifier) which has electronically fast shutter function. Therefore, ICCD with a shorter gate width has been used for the low pressure detection, but in this study, both of spectrometers were applied to investigate the plasma characteristics by effect of environmental pressure.

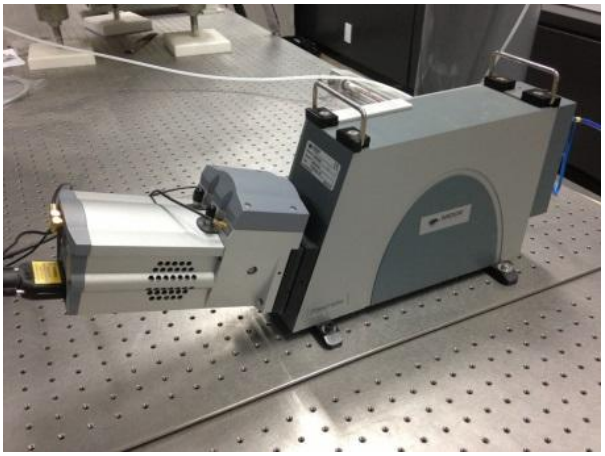

Fig. 2.5 Mechelle spectrometer

Fig. 2.6 Aurora spectrometer

2.3 Other equipments

Timing between laser pulse and spectrometer triggering (gate delay) was controlled by a delay generator (BNC 565 Digital pulse generator). The electric signal output from the flash lamp and Q-switch of the laser and spectrometer was fed to a sampling storage scope (Tektronix TDS1000B) to check the time interval. Several optical equipments such as lens, mirror, beam expander, and optical component with anodizing coating were used for alignment.

The samples were mounted inside of a vacuum chamber of 760 to 10^{-5} torr (Fig. 2.7) where a set of turbo and rotary pump is used to evacuate the chamber. Vacuum chamber is located on a XYZ stage to adjust a sample location.

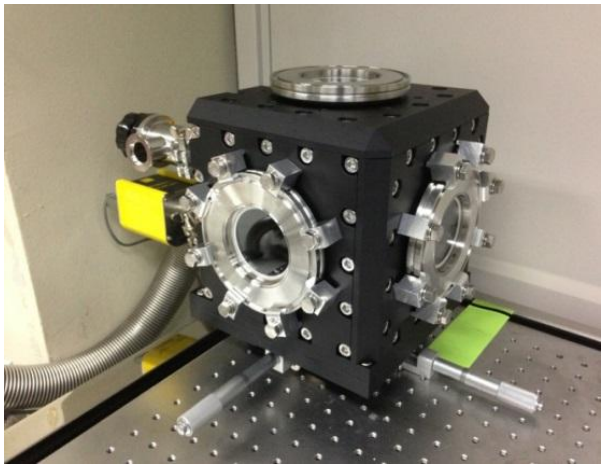

Fig. 2.7 Vacuum chamber

To perform a stand-off experiment, both of refracting telescope (SE102, Kenko) with a 4 inch aperture and the focal length of 500mm (Fig. 2.8) and Schmidt-Cassegrain's telescope (LX200, Meade) with a 8 inch aperture (Fig. 2.9) were used for plasma detection.

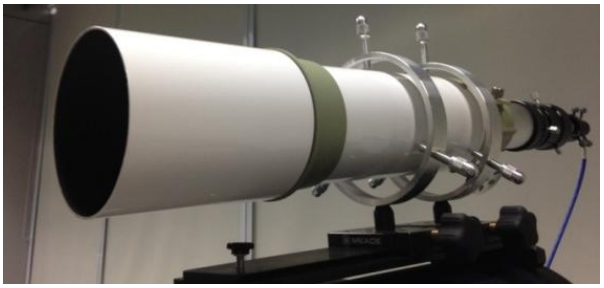

Fig. 2.8 Refracting telescope

Fig. 2.9 Schmidt-Cassegrain's telescope

2.4 Summary

The apparatus used in experiments is summarized in Table 2.1. The detailed conditions are specified in experimental condition part of each experiment.

Table 2.1 Apparatus used in experiments

Device /Sample	Fundamental study	Quantitative analysis	Environment condition	Stand-off detection	Signal enhancement
RT250		○			○
Surelite	○		○	○	
Minilite	○				
Mechelle (ICCD)	○		○	○	
Aurora (CCD)		○			○
Vacuum chamber		○	○	○	○
Telescope				○	
Pulse generator	○		○	○	
Oscillo-scope	○		○	○	
Optical component	○	○	○	○	○
Metal plate	○		○	○	○
Graphite			○		○
CRMs		○		○	○

CHAPTER 3

FUNDAMENTAL STUDY ON EMISSION SIGNAL CONSIDERING EXPERIMENTAL PARAMETER [15]

3.1 Background and objective

The LIBS specification was investigated that is required to build the payload for space exploration based on the effect of LIBS signals toward the characteristics of experimental configuration and laser wavelength.

Strengthening of the LIBS signal in harsh environments is thus the natural objective of the present detection where the plasma generation is inherently difficult. In order to advance signal detection capability, double-pulse LIBS is applied and creatively modified to increase the signal intensity. In addition, the sample and the detector are positioned at several angles to identify optimum conditions at which to perform the detection. This study confirms the existence of optimum configurations for the LIBS system at which strong signals are obtained for objects of arbitrary shape.

The most commonly used laser in LIBS study is Nd:YAG laser that has four types of wavelength. Thus optimum wavelength of Nd:YAG laser proper to space mission was investigated.

3.2 Experimental condition

The experimental apparatus is specified in Table 2.1. The dual-pulse Nd:YAG laser is used for the time differential irradiation of two laser pulses. Timing between two laser pulses (interpulse delay) with respect to the spectrometer triggering (gate delay) is controlled by an independent pulse-delay generator. The excitation wavelength is 532 nm with 25 mJ maximum pulse energy focused on an aluminum plate. When the interpulse delay is zero, the two pulses are emitted simultaneously at a combined energy of 50 mJ. The plasma for LIBS analysis was generated by focusing a laser beam using a 90 mm focal length lens. The optimum delay time is typically one or two microseconds after the plasma initiation. In the case of a double pulse, the interpulse delay is defined by the time between the first pulse and the second pulse. The gate delay and gate width are varied from 0.3 μs (double pulse) to 1 μs (single pulse) and then to 50 μs, respectively. The gate delay is the time between laser irradiation and turning on the spectrometer, and the gate width is the acquisition time of the signal. These temporal elements are important in reducing signal-to-noise ratio and proper detection of the spectrum.

To perform the experiment of wavelength effect, four types of wavelength were considered using Nd:YAG laser with 45 mJ per pulse. Six types of metal samples that contain aluminum, titanium, nickel, copper, tin, zinc and Graphite sample were used. Detection angle is perpendicular to the sample surface except detector angle variation experiment.

3.3 Collinear double pulse test

Using a double pulse LIBS system for stronger coupling of laser energy to the ablated sample allows enhanced emission intensities, lower detection limits, and stronger sustained plasma emission [16-19]. Double-pulse LIBS irradiates two pulse beams in a short time interval : it can be largely categorized as (1) a collinear mode and (2) two orthogonal modes.

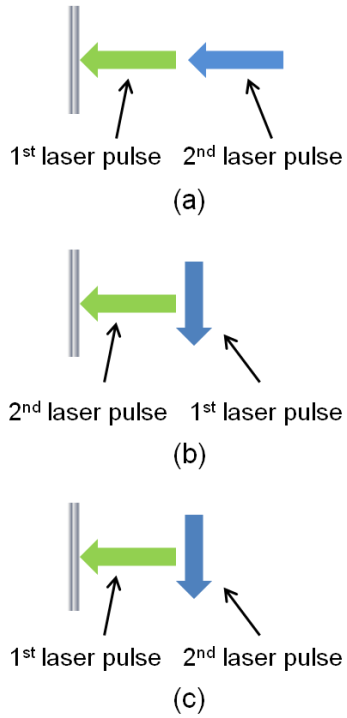

Fig. 3.1 Classification of double pulse LIBS: (a) collinear mode, (b) orthogonal pre-ablation mode, and (c) orthogonal re-heating mode

In the collinear mode, two pulses are irradiated at the same spot on a sample as shown in Fig. 3.1(a), whereas in the orthogonal pre-ablation (Fig. 3.1(b)), the first laser pulse irradiates parallel to the sample surface, generating laser-induced plasma above the sample, while the second pulse generates strong plasma. However, the orthogonal mode always requires an atmosphere to break down the air above the sample and is thus not suitable for vacuum conditions. In addition, the mechanism by which the pre-ablation pulse causes enhanced ablation is not yet clearly understood. Further, in the orthogonal re-heating mode, the first pulse irradiates the target and the second re-heating pulse is propagated parallel to the sample as shown in Fig. 3.1(c). This method can increase electron density and temperature of the plasma.

In the present analysis, we focus on the collinear mode using a single-beam source, which can provide needed simplification and thus weight reduction to the LIBS system by generating double pulses using a single laser.

We performed experiments on the effects of interpulse delay to compare the LIBS signal intensity and the spectrum. The aluminum sample used in this experiment is not a certified reference material: it may contain extra traces of calcium, potassium, and sodium as well as aluminum.

Figure 3.2 shows the signal intensity of the neutral atom (Al I) and first ionized atom (Al II) of aluminum via interpulse delay. Using the double-pulse approach, the signal intensity increases 5 to 20 times at an interpulse delay of 2 μs compared with a single-pulse signal. This happens to both the neutral and

first ionized aluminum atoms. Also, in the case of the first ionized atom (Ca II) of calcium, the maximum intensity appeared at an interpulse delay of 2 μs, as shown in Fig. 3.3. Both results suggest that the optimum signal is observed at the same delay time under identical configurations. More element analysis is desired to identify optimum time delays for LIBS spectra for elements of varying physicochemical properties.

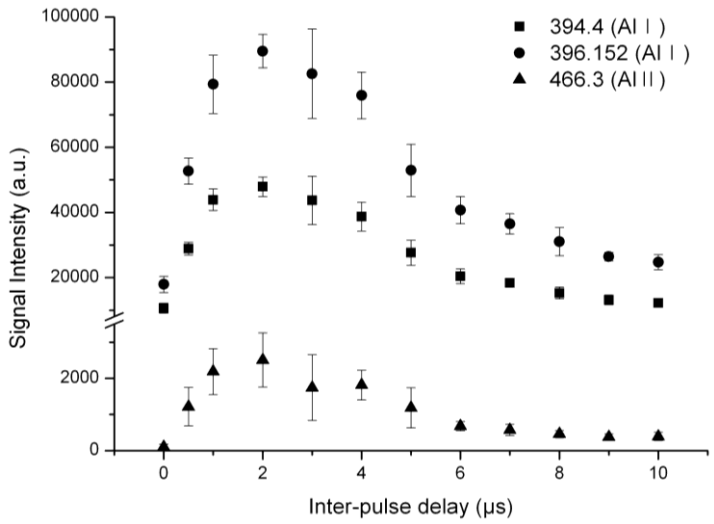

Fig. 3.2 Signal intensity of neutral and first ionized atom of aluminum according to interpulse delay

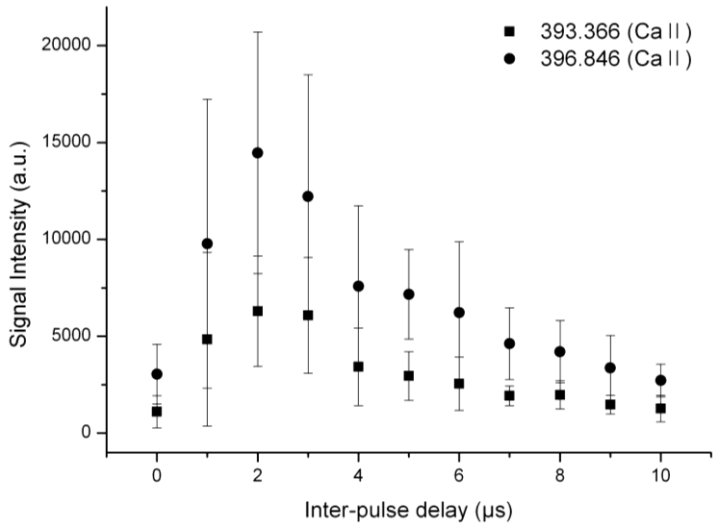

Fig. 3.3 Signal intensity of first ionized atom of calcium according to interpulse delay

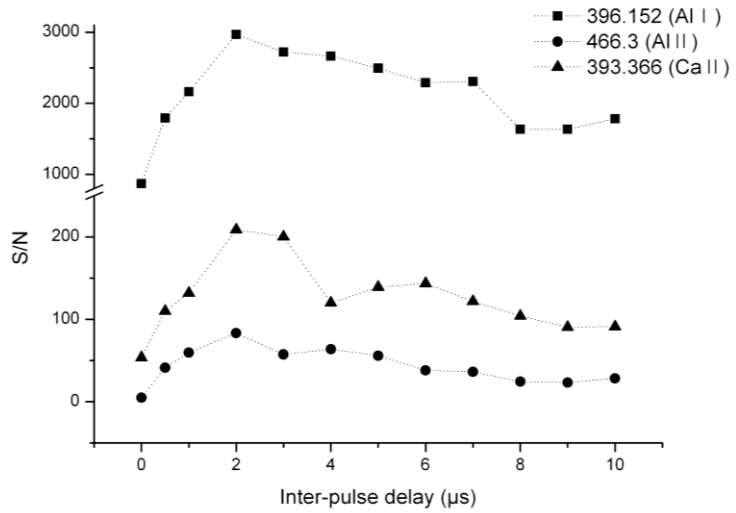

Fig. 3.4 Signal-to-noise ratio of aluminum neutral emission line and aluminum, calcium first ionized emission line

Figure 3.4 shows the signal-to-noise ratio of the aluminum neutral emission line and the aluminum, calcium first ionized emission line. The range from 349.5 to 350.5 nm is interpreted as the noise (namely background) because there is no emission line of a particular element. The signal-to-noise ratio is enhanced at an interpulse delay of 2 μs, similar to the signal intensity. The limit of detection is obtained using the calibration curve. Without presenting the calibration curve, however, one can still deduce approximate limits of detection from the signal-to-noise ratio, such that the detection limit is also improved by the double-pulse approach.

3.4 Effect of sample and detector angle

3.4.1. Sample angle variation

In space resource-detection via LIBS, it is imperative to maintain accurate signals at all times, regardless of the sample shape. A sample of arbitrary shape cannot be irradiated with the laser beam at an angle perpendicular to its surface, as illustrated in Fig. 3.5. To investigate this effect, the angle of sample is adjusted to simulate a sample of arbitrary shape. The energy is set to 50 mJ/pulse as only a single pulse is used in this experiment. The angle of the sample is varied from its zero point, defined as beam–surface perpendicular to the sample. In the case of varied angle of sample, the irradiance and the effective surface of the plasma detection affect the signal intensity. It is commonly known that irradiance has a great effect on the LIBS spectrum. In

this experiment, as the angle changes, the signal intensity also changes while each spectrum maintained its peak.

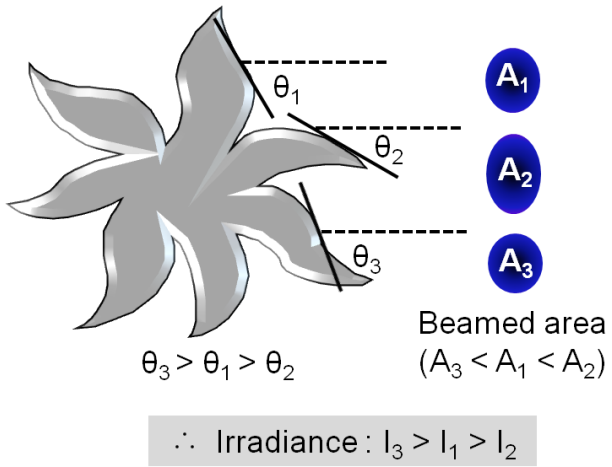

Fig. 3.5 Angle and irradiance variation from sample of arbitrary shape

Figure 3.6 illustrates that an optimum irradiance with an enlarged area of detection of the plasma is received at 5 degrees sample angle in the case of aluminum. However, both potassium and sodium show maximum signal intensity at 30 degrees. The reason for the difference is the variation in the emission wavelength and the mass of each element, for instance. While there is a clear optimum angle of sample for Al at 5 degrees, it is not entirely clear whether there is only one angle that provides maximum intensity for both potassium and sodium. The plasma structures of these elements are believed to be ‘‘spread’’ as compared to Al.

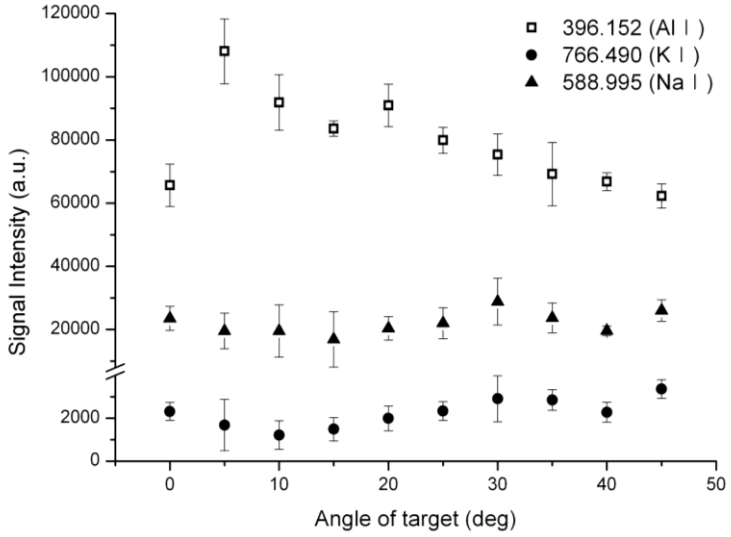

Fig. 3.6 Signal intensity versus angle of sample (Al, K, Na)

Figures 1 and 6 in Ref. [20] provide the different spectrum and elemental distributions inside the plasma. Particularly, each map of Fig. 6 in Ref. [20] was obtained under different focusing conditions. Generally, these maps show that zinc is present at an outer shell and in the ‘‘tail’’ of the plasma, while copper is present mainly in an inner shell. As a result, the position of each element changed according to experimental conditions. Therefore, the signal intensity of each element is also changed, and it can cause a different optimum sample angle for a specific element.

Another cause of elemental variation can be explained by breakdown threshold. As shown in Fig. 3.5, the irradiance of laser energy is in inverse proportion to angle of sample. K and Na can be ablated by lower irradiance

because their ionization potentials are higher than Al and Ca, in other words, they have lower breakdown threshold. Therefore signal intensities of K and Na are not significantly different according to irradiance change.

3.4.2 Detector angle variation

The angle at which the detector is placed in the signal collection is directly related to the detection part of the plasma. If the cylindrical plasma light is detected from the parallel direction to the sample, the tail of the plasma may not be collected accurately. Furthermore, as the angle of the detector becomes large, the center of the plasma can be difficult to detect.

In the present test of aluminum and calcium, a range of 10 to 15 degrees shows the best angles for the detector under the conditions shown in Fig. 3.7(a). On the other hand, different optimal angles are noted for the results of sodium and potassium as shown in Fig. 3.7(b).

The plasma structure will affect these results: each element is located at a different place in the plasma structure according to physical and chemical properties. This means that there exists an optimal angle at which a specific element of a test sample may be detected with stronger signal intensity. To use Fig. 6 in Ref. [20] for example, zinc and copper will have different optimum detection angles, because the position of each element is changed. Most of elements are detected center of the plasma where the temperature is very high while elements with low boiling point located in the outer shell. The angle

variations of both the sample and the detector have shown effective in distinguishing samples of similar physical properties that include emission wavelengths and mass.

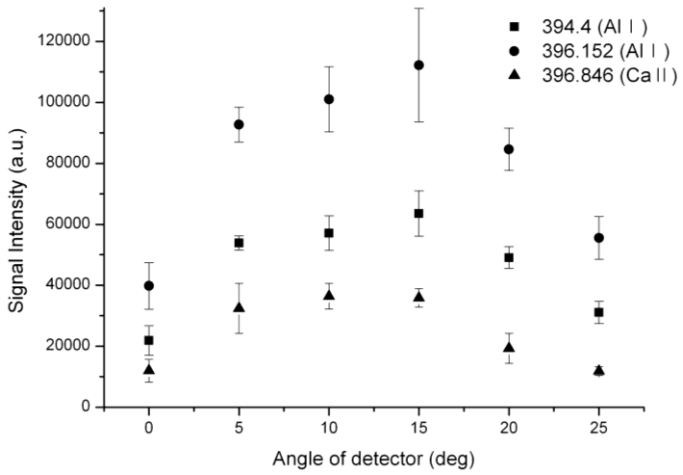

(a)

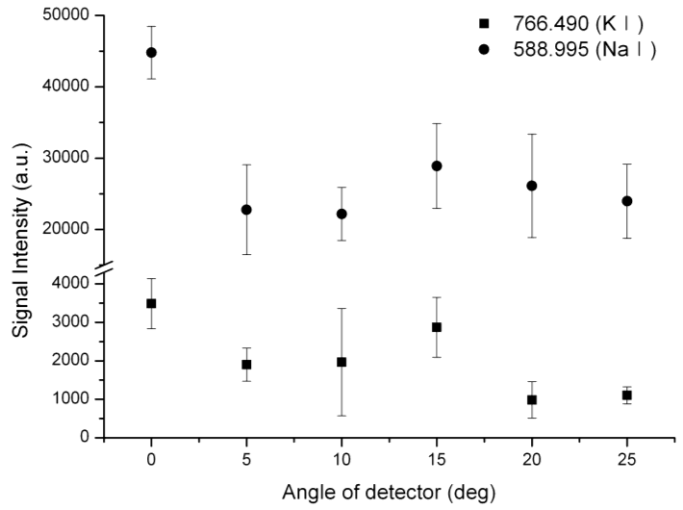

(b)

Fig. 3.7 Signal intensity versus angle of detector

(a) Al and Ca, (b) K and Na

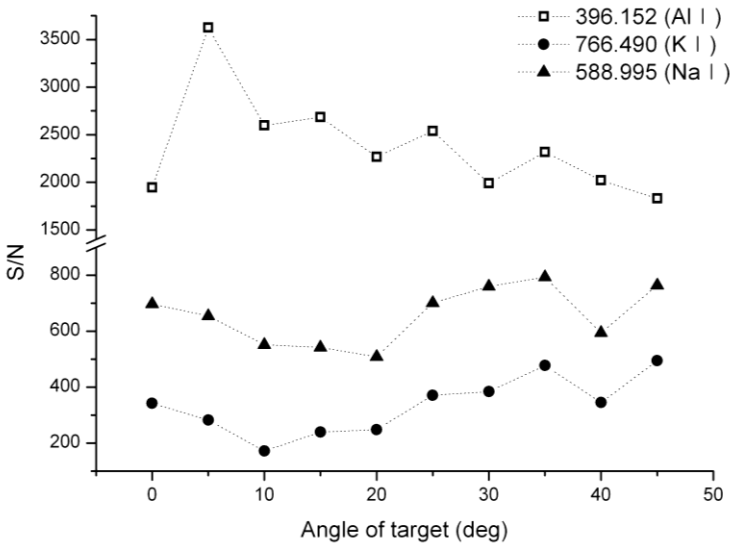

(a)

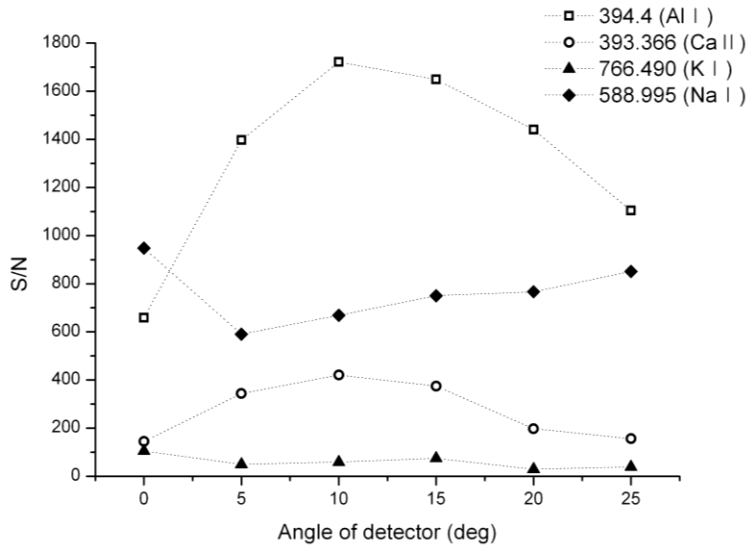

(b)

Fig. 3.8 Signal-to-noise ratio of emission line

(a) sample variation, (b) detector variation

Figure 3.8 shows the signal-to-noise ratio of the emission line of (a) sample and (b) detector variation. The mean value of two areas from 349.5 to 350.5 nm and from 790 to 791 nm was employed as the noise because we inferred that long or short wavelengths will affect the background intensity. The signal-to-noise ratio changed similarly to a variation in the signal intensity, according to sample and detector angles. Therefore the angle variation effectively improved the signal intensity.

To test whether measured potassium and sodium truly have come from the sample, we monitored the K and Na intensity with multiple laser pulses. The surface of the sample was wiped with a lens paper each time to remove any surface contaminants. Then data associated with the first pulse at each location was ignored to provide higher precision of the measurements. Thus, the potassium and sodium are believed to come from the aluminum sample.

3.5 Optimizing the wavelength of laser

A Nd:YAG laser typically emit light with a wavelength of 1064 nm, in the infrared. The high-intensity pulses may be efficiently frequency doubled to generate laser light at 532 nm, or higher harmonics at 355 and 266 nm. In this study we investigated optimum wavelength of Nd:YAG laser for space mission.

Plasma characteristics such as signal intensity, lifetime, and detectable element are dependent on wavelength of laser. When using infrared laser

(1064 nm), the emissive plasma plume expansion tends to propagate in the direction of the laser beam, while the ultraviolet (266 nm) laser creates an approximately spherical plume which is relatively more confined than the plume created by the IR laser [21]. Therefore, if the infrared laser plasma is observed in a collinear fashion, the top of the plasma plume can shield the emissions coming from the bottom of the plume, while the ultraviolet laser plasma may be observed satisfactorily from any direction. This shielding of emissions is thus avoided by observing the infrared laser plume orthogonally from the laser axis like our setup.

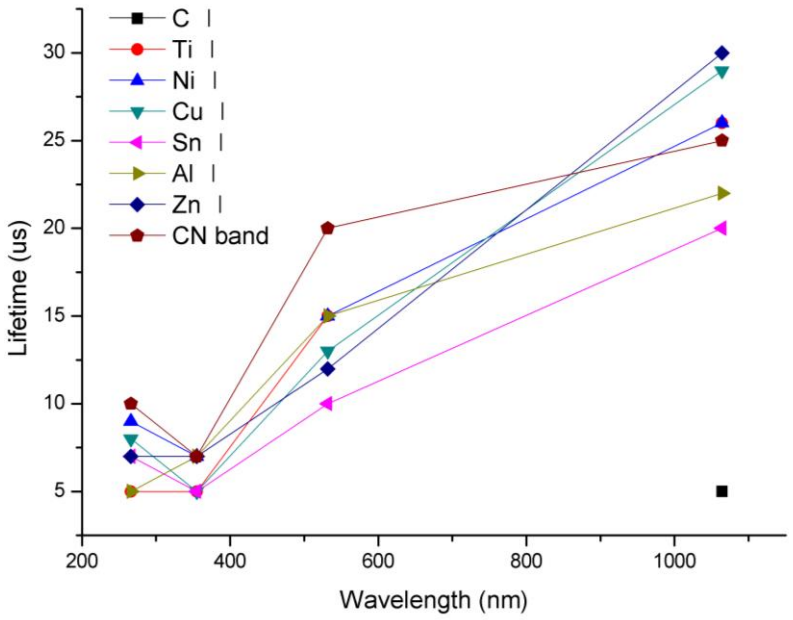

Fig. 3.9 Plasma lifetime according to wavelength of laser

Figure 3.9 shows the plasma lifetime caused by different wavelength of laser. In this experiment, 1064 nm was optimum wavelength. Also 1064 nm is fundamental wavelength of Nd:YAG laser which does not need additional payload such as harmonic generator and dichroic mirror thus proper wavelength for space mission.

.

CHAPTER 4

QUANTITATIVE ANALYSIS [22]

4.1 Background and objective

The quantitative analysis is required to estimate the concentration of unknown samples not only in the space mission but also for many applications such as industry fields, pollution monitoring, and analysis of nutrient in foods. This study provides a method for more accurate quantitative analysis by overcoming the matrix effect that can be applied various spectroscopic methods as well as a LIBS technique.

The accuracy of calibration curves can be affected by the matrix due to changes in ablation behavior as a function of the matrix composition. Matrix effects cause changes in emission line signal intensity even though samples may contain the same concentration of an element. Possible causes of matrix effects include changes in the amount of ablated mass between samples, quenching of elements in the laser-induced plasma, and changes in the plasma conditions (temperature and electron number density) due to changes in the sample composition. Addressing matrix effects is an important issue in quantitative analyses, for all analytical technologies.

As a step toward quantitative analysis, many researchers are studying the LIBS analysis in the context of generating calibration curves which indicate

the relation between signal intensity and concentration. One way to build up the calibration curve is to use either certified reference materials (CRMs) that have the certified concentration [23-25] or non-certified materials with relatively well-known concentration [26, 27]. Another way is to compare the LIBS data with the result of comparative analysis such as ICP-OES (ICP-AES) [28, 29] and X-ray fluorescence [30]. The accuracy of calibration curves can be affected by the matrix effect which is caused by difference in the chemical compositions of samples. Although samples may contain the same concentration of a certain element, their signal intensities are not always identical. Hence, correcting the matrix effect has been an important issue in quantitative LIBS analyses.

One way of correcting the matrix effect is by normalization of the spectrum. Gornushkin et al. [31] reported that the surface density normalization method combined with analysis of the mechanical effect of the ablated weight provides a simple solution to deal with the matrix effect. Huang et al. [32] also suggested that normalization of the LIB emission by the current correlated analysis is a convenient way of suppressing the signal fluctuation and improving the LOD determination.

Also, plasma temperature-related correction method is proposed. Dettman et al. [33] and Bulajic et al. [34] described that a simple partial local thermodynamic equilibrium model could reduce the matrix effect to handle changes in sensitivity driven by the plasma temperature. Zhang et al. [35]

utilized the calibration method with fixed plasma temperature in order to minimize the matrix effect. The chemometrics (principal component analysis, partial least squares, or principal component regression) is also commonly applied in quantitative LIBS analysis to compensate for this matrix effect. Anderson et al. [36] used partial least squares regression to improve the accuracy of quantitative chemical analysis of LIBS. Doucet et al. [37] presented the use of chemometrics as a multivariate regression tool to compensate for matrix effects. They used multilinear regression, principal component regression, and partial least square regression and claimed that chemometrics coupled with LIBS was a suitable combination for the quantitative analysis of aluminum alloys. A good application of PCR and PLS models to pharmaceutical ingredients can be found in [38].

In this study, we carried out quantitative analysis of the LIBS signals from CRM samples. In order to minimize errors due to the matrix effect, we used 21 CRMs that belong to different categories of food, clay, sludge, steelmaking alloy, and geochemical and agricultural materials. The large number of CRM samples will make sure that various matrix effects be present in the present analysis. It is expected that the calibration curve of each category and/or material will show characteristic linear trend according to its chemical and physical property. Furthermore, principal component analysis (PCA) was used for a rapid identification and discrimination of the samples. The PCA result was compared with the calibration curve to establish quantitative LIBS

procedure for the analysis of various CRM samples. Also multivariate analysis based on linear regression model was applied to correct the matrix effect.

4.2 Experimental condition

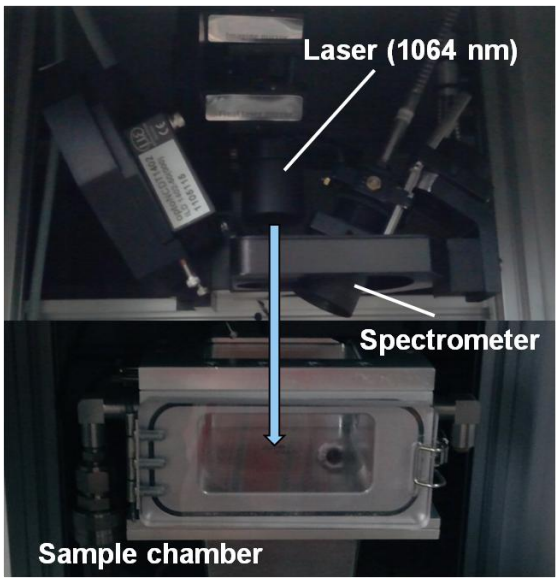

Fig. 4.1 Test section of a commercial LIBS system (RT250-Ec)

The experimental apparatus is specified in Table 2.1. As shown in Fig. 4.1, each part of LIBS system (laser, spectrometer, optical components, and sample chamber) is integrated and aligned in RT250-Ec device. The laser beam was focused onto the sample surface by a lens of 50 mm focal length. Time delay of the spectrometer was 1 μs, and the gate width was 1.05 ms. To

collect plasma, a lens of 50 mm focal length was used. Samples were placed in the chamber at room pressure and temperature on a XYZ stage. The laser beam was focused on the sample surface and fired on 6 locations with 10 shots for each location.

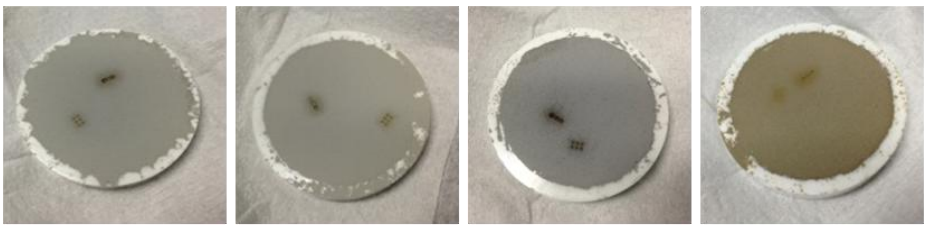

Fig. 4.2 Pelletized sample of geochemical reference materials

(a) SCo-1, (b) GSP-2, (c) QLO-1, (d) W-2

The 21 powdered CRM samples from NIST (National Institute of Standards and Technology) and USGS (United States Geological Survey) were selected as standard materials for space exploration shown in Table 4.1. Those samples were chosen from 6 categories of interests, which are agricultural materials, foods, clays, soils and sediments, steelmaking alloys, and geochemical reference materials. Each of the samples was mixed with paraffin binder at a proportion of 10% to 100% concentration by the difference of 10% and was pelletized (Fig. 4.2) with 10 tons of pressure, 2.5 minutes of dwell time and 1.5 minutes of release time (Spex model 3635). The paraffin binder contains

only hydrogen and carbon (C_nH_{2n+2}) so that it can adjust the concentration without any effect on the result as well as bonding the powder sample.

Table 4.1 List of 21 SRM samples of varying constituents

CRM	Description	
NIST 1515	Apple leaves	Agricultural
NIST 1547	Peach leaves	
NIST 1570a	Trace elements in Spinach leaves	
NIST 1573a	Tomato leaves	
NIST 1575a	Trace elements in Pine needles	
NIST 1566b	Oyster tissue	Foods
NIST 1567a	Wheat flour	
NIST 1568a	Rice flour	
NIST 1577c	Bovine liver	
NIST 97b	Flint clay	Clays
NIST 98b	Plastic clay	
NIST 679	Brick clay	
NIST 2780	Hard rock mine waste	Soils, sludge, sediments
NIST 2782	Industrial sludge	
NIST 59a	Ferrosilicon	Steelmaking alloys
NIST 64c	Ferrochromium, high carbon	
NIST 68c	Ferromanganese, high carbon	
USGS GSP-2	Granodiorite	Geochemical reference
USGS QLO-1	Quartz Latite	
USGS SCo-1	Shale-Cody	
USGS W-2	Diabase	

Nine elements (Al, Ca, Mg, Ti, Si, Fe, K, Na, Mn) in each sample were analyzed. We based our selection of the specific emission lines on the peak intensity, interference with other emission lines, and spectrometer saturation. The selected peaks are as follows: Al (396.152 nm), Ca (422.6727 nm), Mg (285.213 nm), Ti (334.941 nm), Si (288.158 nm), Fe (373.4864 nm), K (766.490nm), Na (588.995 nm), and Mn (403.076 nm).

4.3 LIBS spectra

Figure 4.3 shows the LIBS spectra of several CRM samples. It is possible to classify the sample into groups based on their composition from the LIBS spectra. For example, food and agricultural samples such as NIST1515, NIST1573a, NIST1566b, and NIST1567a (first four graphs in Fig. 4.1) are seen distinct from the signals of the other CRM samples of clays, soils, and steelmaking alloys. Also the same samples of food and agricultural materials can be subdivided into two minor groups (NIST1515, NIST1573a / NIST1566b, NIST1567a) according to the existence of CN band at 388 nm. However, in the cases of NIST1515 and NIST1573a, they are indistinguishable through LIBS spectra since both samples have similar chemical components. Thus we make use of the chemometrics to address the need for a refined discrimination.

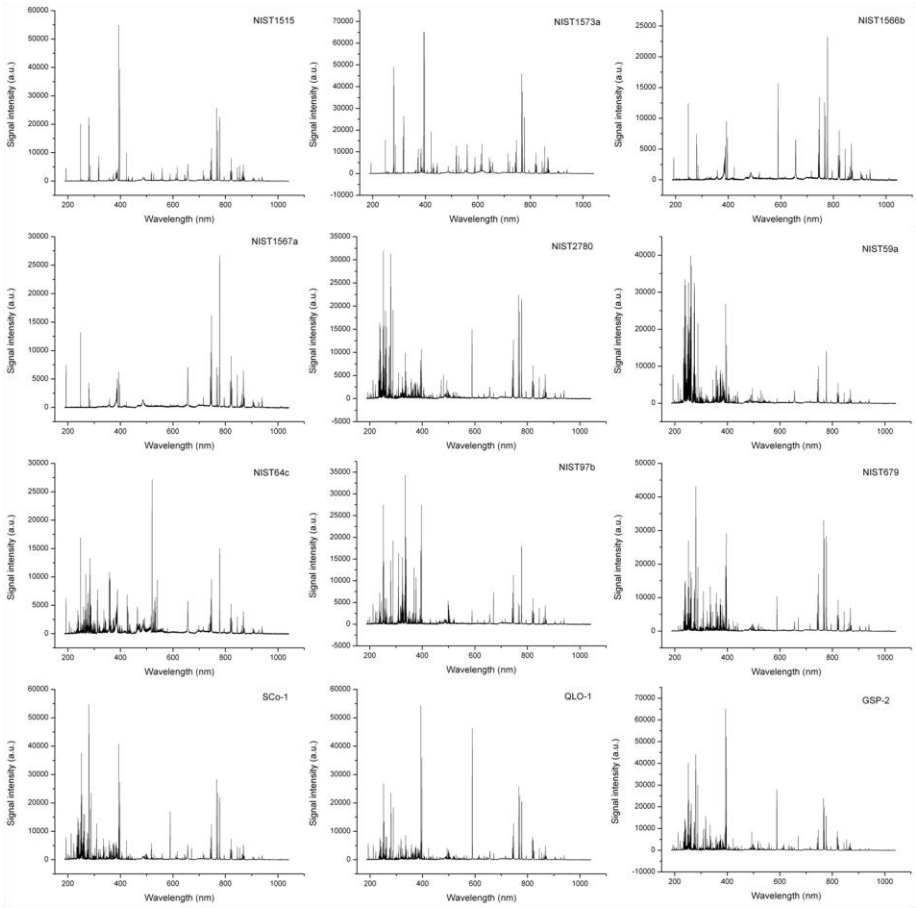

Fig. 4.3 LIBS spectra of several SRM samples. First four graphs (NIST 1515, 1573a, 1566b, 1567a) are clearly distinguishable from the rest

4.4 Principal component analysis (PCA)

Figure 4.4 shows the PCA result from 21 CRM samples where 90% concentration samples are composed of the CRM and the binder in the proportion of 9:1. Some samples were hard to pelletize without the use of a binder as such to mix with the paraffin binder at 90% concentration was

needed. The CRM samples that were indistinguishable from LIBS spectra were discriminated using the PCA procedure, as one could see from the results for NIST1515 (red square) and NIST1573a (yellow triangle). Four distinct groups of food and agricultural, clay and soil, steelmaking alloy, and sludge are shown in Fig. 4.4.

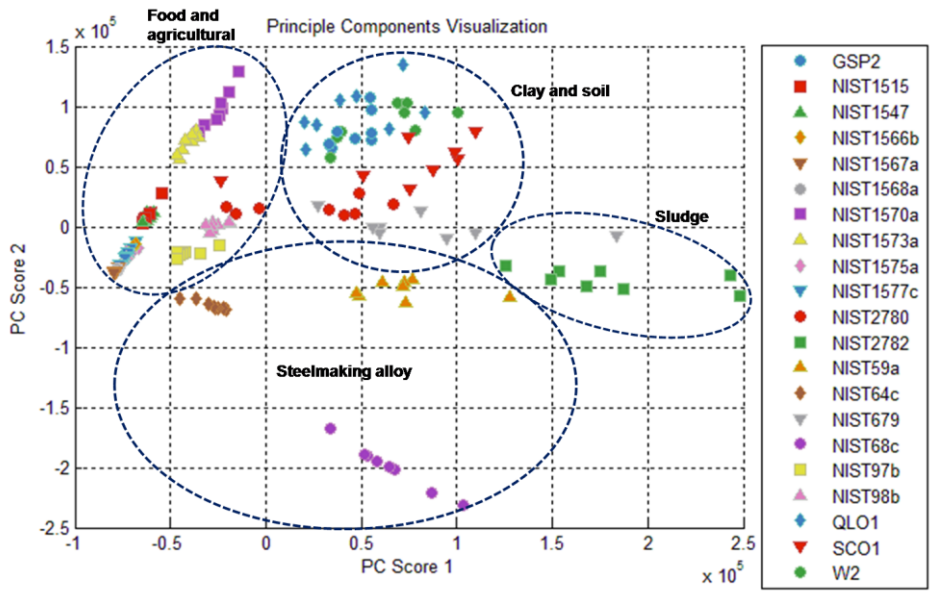

Fig. 4.4 PCA result from 21 SRM sample of 90% concentration

The PCA results show clear separation of each group especially in the case of steel making alloy where all are comprised of different elements. Some scatterings are present in the PCA plot due to a possible incomplete mixing of CRM and paraffin binder due to their large particle size (for example,

NIST68c, NIST2782, NIST59a, SCo-1, NIST2780). The PCA results seem to be clustered altogether in some cases of NIST1567a, NIST1568a, NIST1577c, NIST1566b, and NIST1575a. One can assume that they all have similar major elemental composition.

As mentioned in the experimental setup, each sample was mixed with the paraffin binder at a proportion of 10% to 100% concentration at an increment of 10%. Therefore, the dispersion of PCA results of all samples converges at the origin according to the decrease of the concentration as shown in Fig. 4.5, which suggests that the samples at low concentration have similar characteristics.

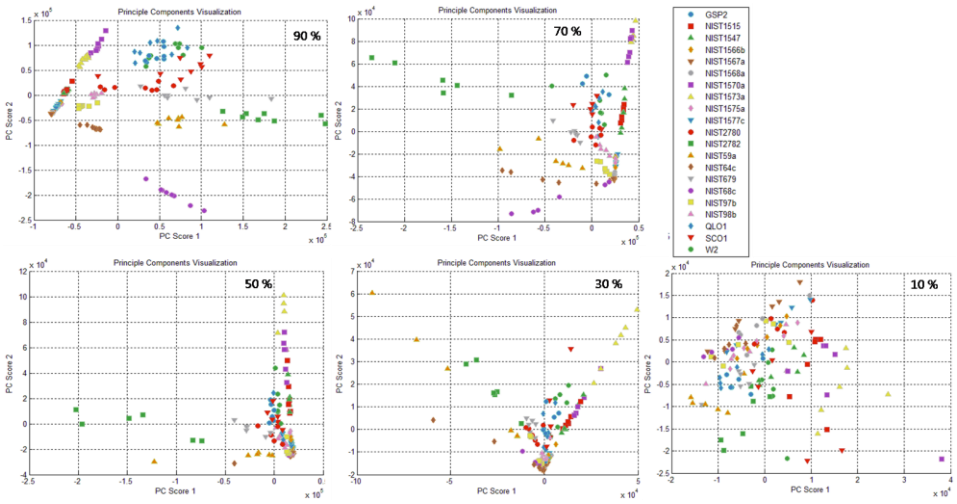

Fig. 4.5 PCA results according to the concentration

4.5 Univariate analysis

Building a database of elemental calibration curve is needed before carrying out the quantitative analysis of an unknown sample. Background subtraction was applied in order to deal with the continuum of each spectrum. The area of emission peak with subtraction of the background adjacent to emission line was used as the signal intensity. The concentration of the element is shown in Table 4.2 with the tested CRM samples. The combination of chemometrics and calibration curves of pure CRM samples with respect to the known sample intensities was performed as a solution to the matrix effect [31-38]. Similar groups emerged from the PCA data (Fig 4.4). We categorized 3 to 7 groups of elements with the analyzed calibration curves of the whole samples, since the characteristics of each element was not considered in the PCA results in Fig. 4.4.

Table 4.2 Concentration of CRMs [39]

(Concentrations are in mg/kg,

unless noted by a single asterisk for mass fraction, in %)

CRM	Mg	Si	Ca	Ti	Fe	Al	K	Na	Mn
1515	0.271*		1.526*		(83)	286	1.61*	24.4	54
1547	0.432*		1.56*		(218)	249	2.43*	24	98
1570a	(0.89*)		1.527*			310	2.903*	1.818*	75.9
1573a	(1.2*)		5.05*		368	598	2.70*	136	
1575a	0.106*		0.25*		46	580	0.417*	63	488
1566b	0.1085*		0.0838*		205.8	197.2	0.652*	0.3297*	18.5
1567a	0.040*		0.0191*		14.1	5.7	0.133*	6.1	9.4
1568a	0.056*		0.011*		7.4	4.4	0.1280*	6.6	20.0
1577c	620	(6)			197.94		1.023*	0.2033*	10.46
97b	0.113*	19.81*	0.0249*	1.43*	0.831*	20.76*	0.513*	0.0492*	47
98b	0.358*	26.65*	0.0759*	0.809*	1.18*	14.30*	2.81*	0.1496*	116
679	0.7552*	24.34*	0.1628*	0.577*	9.05*	11.01*	2.433*	0.1304*	(1730)
2780	0.533*	(31*)	0.195*	0.699*	2.784*	8.87*	3.38*	0.221*	462
2782	0.26*	(20.3*)	0.67*	880	26.9*	1.37*	0.32*	1.30*	(300)
59a		48.10*	0.042*		50.05*	0.35*			0.75*
64c		1.22*		0.02*	24.98*				0.16*
68c		0.225*			12.3*				80.04*
GSP-2	0.58*	31.3*	1.50*	0.40*	3.43*	7.88*	4.48*	2.06*	320
QLO-1									
SCo-1									410
W-2									

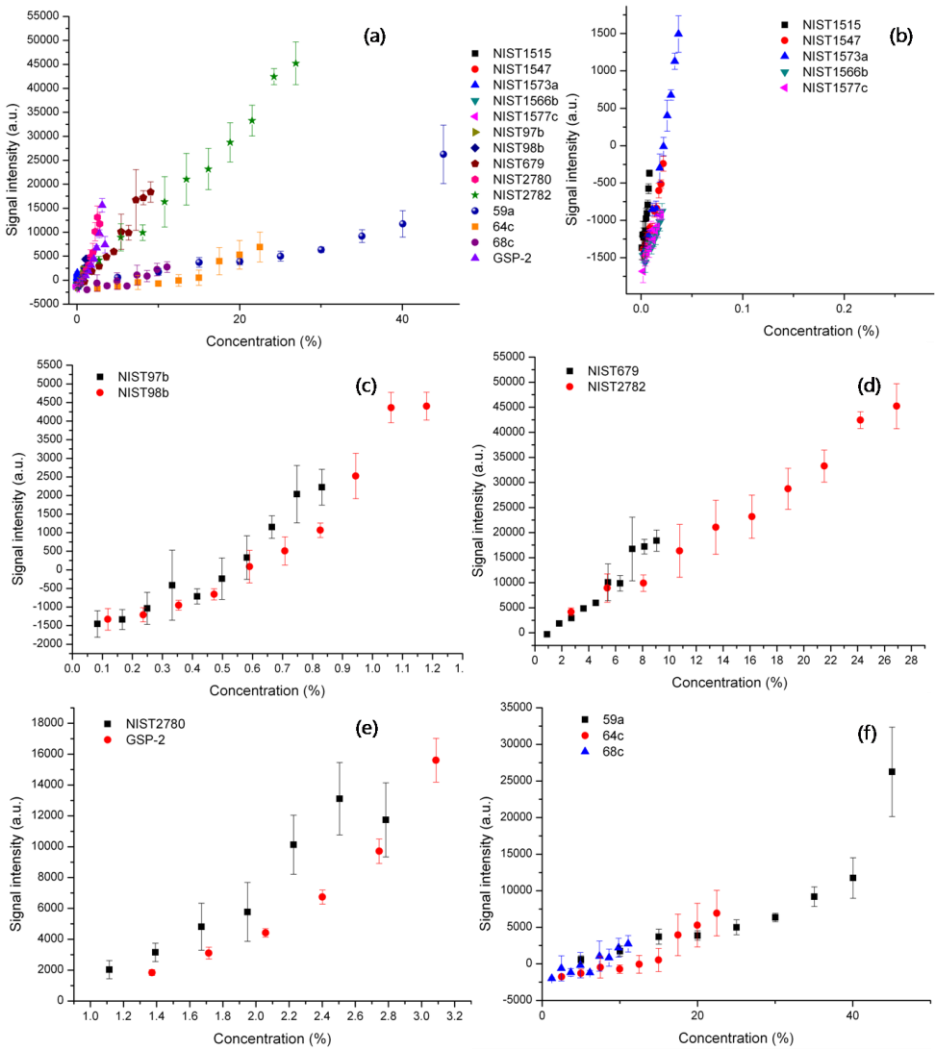

Fig. 4.6 Categorization of Fe by calibration curves of all SRM samples. 5 distinct groups ((b)~(f)) emerged from the combined graph (a)

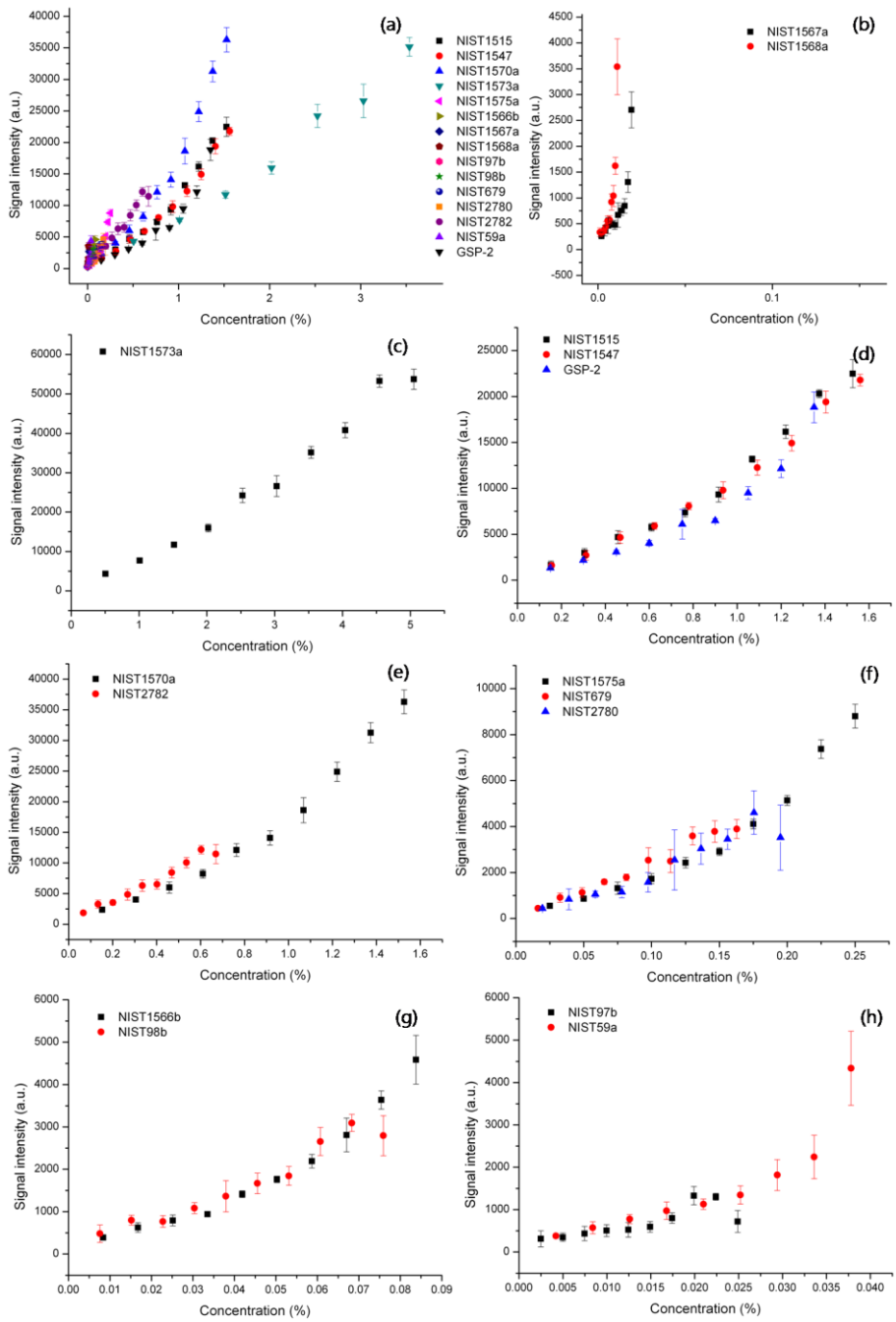

Fig. 4.7 Categorization of Ca by calibration curve of all SRM samples. 7 distinct groups ((b)~(h)) emerged from the combined graph (a)

Figure 4.6 shows 5 groups (b)~(f) separated from the combined calibration curve of Fe (Fig. 4.6(a)). The concentration in all of the calibration curves is the total concentration of element in the sample. Figure 4.6 is consistent with Table 4.1 and PCA results in Fig. 4.4, as classified into (b) food & agricultural material, (c) clay, (d) clay & sludge, (e) granite type, (f) steel making alloy. Figure 4.7(a), a combined calibration for Ca, was not categorized as well, while food, clay, steel making alloy groups were mixed with (b)~(h) groups altogether. Table 4.3 shows complete classification of CRM samples with respect to elements from calibration curve. It can be inferred from Table 4.3 that the effect of particular elements must be taken into account when performing quantitative LIBS analysis, in order to build accurate calibration curves. This is because the PCA results were not applicable to some of the elements such as K, Mg, and Ca.

Table 4.3 Groups for each element from calibration curve

Element	SRM Samples	Groups
Ti	1. NIST97b	: clay
	2. NIST98b, NIST679, NIST2780	: clay & granite
	3. GSP-2	: granite
Si	1. NIST59a	: alloy
	2. NIST2780, GSP-2	: granite
	3. NIST97b, NIST98b, NIST679, NIST2782	: clay & sludge
Na	1. NIST2782, GSP-2	: sludge & granite
	2. NIST1570a, NIST1566b, NIST1577c	: agricultural & food
	3. NIST97b, NIST98b, NIST679, NIST2780	: clay & granite
	4. NIST1515, NIST1547,	: agricultural & food

	NIST1573a, NIST1575a, NIST1567a, NIST1568a	
Fe	1. NIST59a, NIST64c, NIST68c 2. NIST2782, NIST679 3. GSP-2, NIST2780 4. NIST98b, NIST97b 5. NSIT1515, NIST1547, NIST1573a, NIST1566b, NIST1577c	: alloy : clay & sludge : granite : clay : agricultural & food
Al	1. NIST97b 2. NIST98b, NIST679 3. NIST2780, NIST2782, GSP-2 4. NIST59a 5. NIST1515, NIST1547, NIST1573a, NIST1575a, NIST1567a, NIST1568a, NIST1570a, NIST1566b	: clay : clay : sludge & granite : alloy : agricultural & food
Mn	1. 68c 2. 59a, 64c 3. NIST1575a, SCo-1, GSP-2	: alloy : alloy : agricultural & soil, granite
K	1. NIST98b, NIST2780, GSP-2 2. NIST679, NIST1547 3. NIST1570a, NIST1573a, NIST1515, NIST1577c 4. NIST97b, NIST1566b 5. NIST1575a, NIST2782 6. NIST1567a, NIST1568a	: clay & granite : clay & food : agricultural & food : clay & food : agricultural & sludge : food
Mg	1. NIST1573a 2. NIST1570a, NIST679 3. NIST2780, GSP-2, NIST1547, NIST98b 4. NIST1515, NIST2782, NIST97b 5. NIST1575a, NIST1566b 6. NIST1567a, NIST1568a	: agricultural : agricultural & clay : food & clay, granite : food & sludge, clay : agricultural & food : food
Ca	1. NIST1573a 2. NIST1515, NIST1547, GSP-2 3. NIST1570a, NIST2782 4. NIST1575a, NIST2780, NIST679 5. NIST98b, NIST1566b 6. NIST59a, NIST97b 7. NIST1567a, NIST1568a	: agricultural : agricultural & granite : agricultural & sludge : agricultural & granite, clay : food & clay : alloy & clay : food

Figure 4.8 shows linear fittings of Ca whose characteristics is randomly grouped. It is not categorized with specific materials, rather the result is verified to be accurate having a high correlation coefficient, R^2.

Figure 4.9 is a calibration curve of Fe. It shows high correlation coefficient amongst all the groups except for group 5 that is comprised of food and agricultural materials. The experimental error of group 5 seems to be higher than other groups since it has lower concentration of Fe. This suggests raising the sensitivity by considering the low pressure circumstances and the optimized layout of the experimental setup to detect minor elements.

Figure 4.10 corresponds to the calibration curves of Si and Ti. We applied polynomial fittings because Si and Ti tend to have nonlinear curves. The result was successful as they were well categorized with the expected groups of Table 4.3. Although polynomial fitting can achieve high correlation coefficient, it makes it more difficult to estimate concentrations beyond the range of calibration curves than linear fitting. Therefore, linear fitting is a preferred method if the error is not so critical.

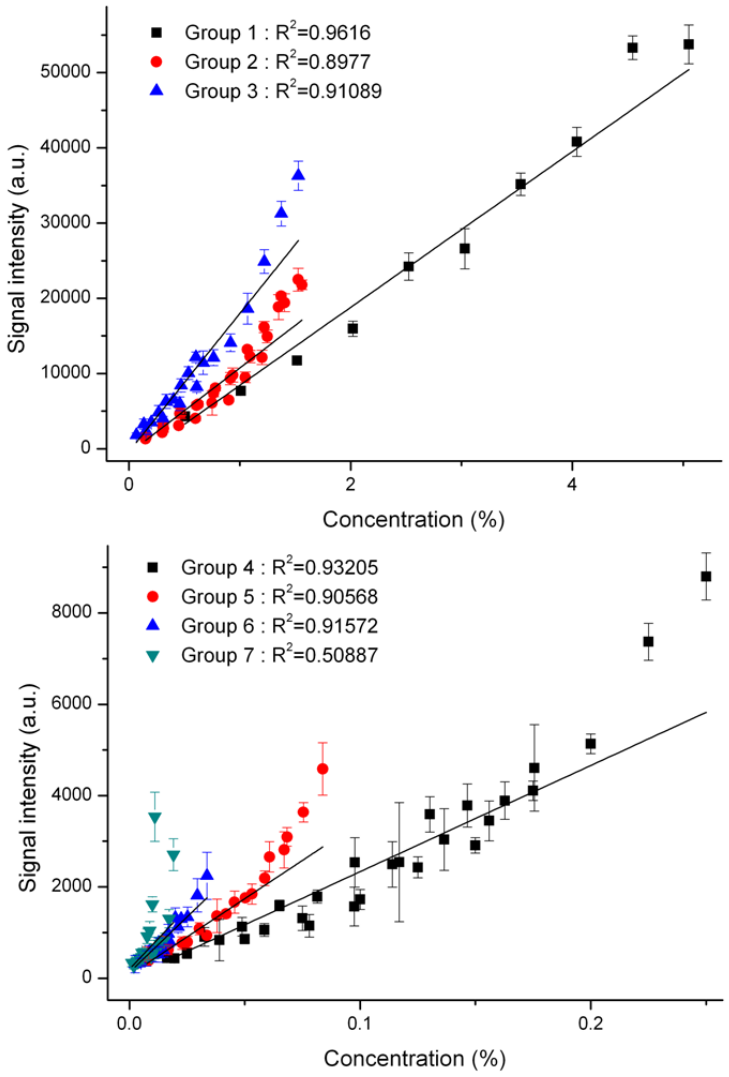

Fig. 4.8 Calibration curves of Ca showing 7 groups from Table 4.3

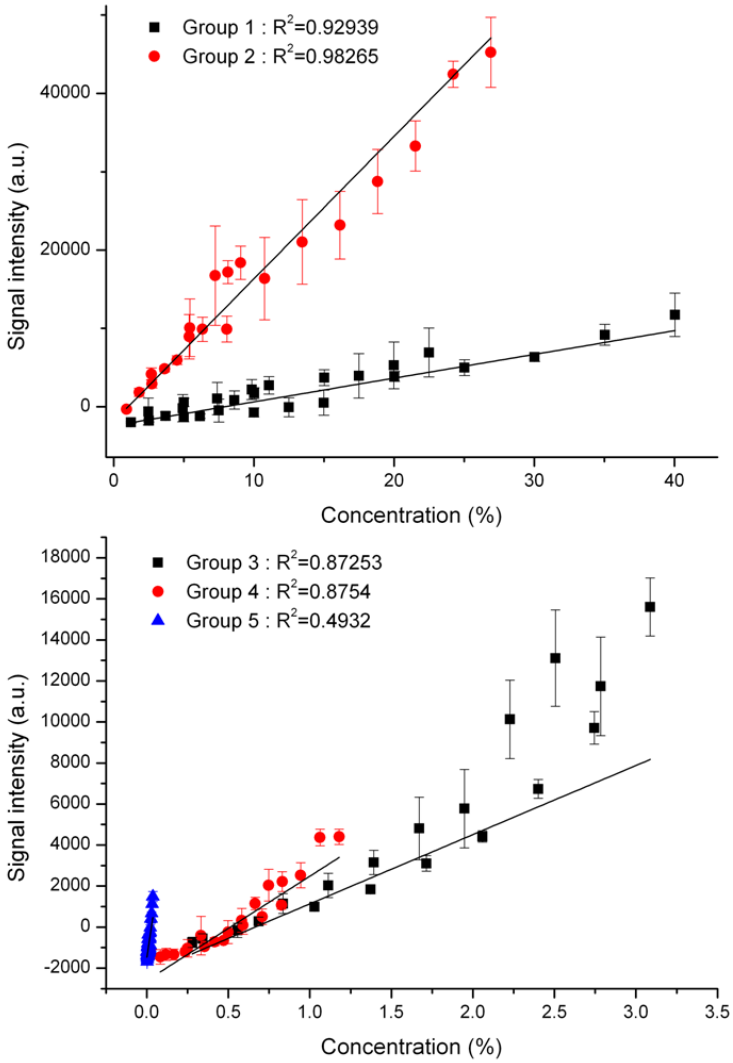

Fig. 4.9 Calibration curves of Fe showing 5 groups from Table 4.3

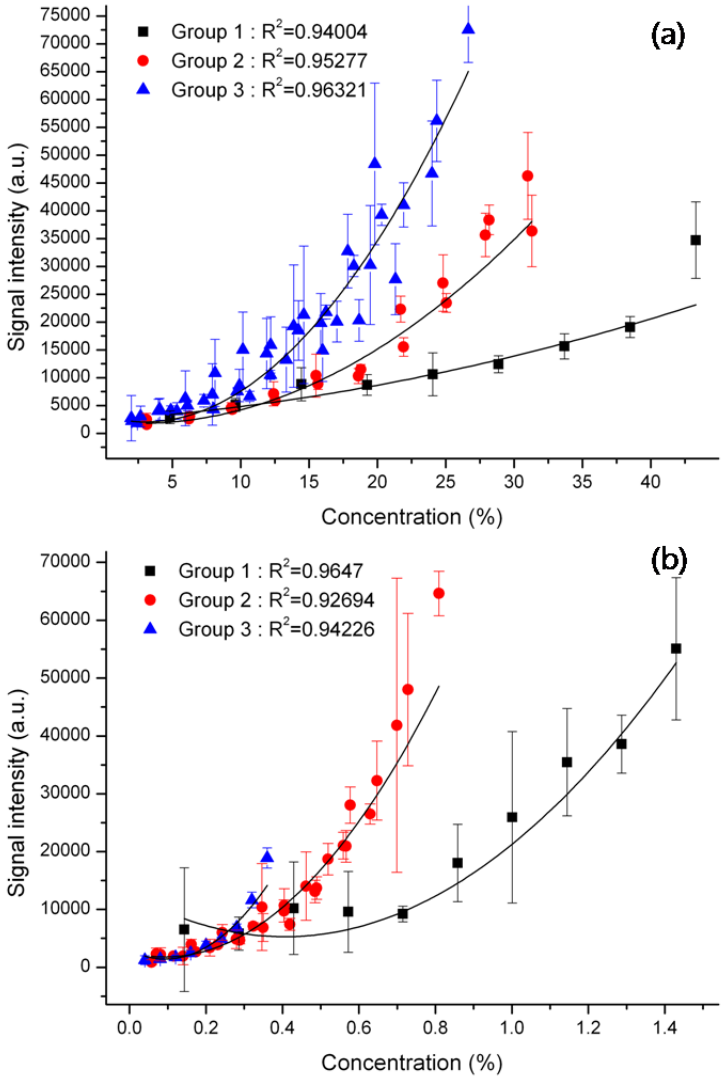

Fig. 4.10 Calibration curves of (a) Si of 3 groups and

(b) Ti of 3 groups from Table 4.3

4.6 Multivariate analysis

Figure 4.11 shows the univariate calibration curve of Ca which indicates the relation between signal intensity from LIBS spectra and concentration of sample. One or more standard samples are required in order to establish the calibration curve. The relation between signal intensity and concentration is usually represented by linear relation as shown in Eq. (4.1).

$$Y = mX + b \qquad \text{- (4.1)}$$

(m : slope, b : intercept, X : concentration, Y : measured signal intensity)

Univariate calibration uses the slope and intercept by calibration curve to obtain the concentration of unknown samples. The standard samples that are used to construct the calibration curve should be have a similar chemical composition, matrix-matched standards. As shown in Fig. 4.11, Ca calibration curves display different slope as a function of the matrix. Thus this situation requires matrix-match between the unknown samples and the standard to successfully determine analyte concentrations. However standard samples could not cover every type of unknown samples. Besides univariate method considers only the signal intensity to obtain the calculated concentration, thus this approach can miss changes happening in other parts of the spectrum that can reflect changes in the plasma conditions, etc.

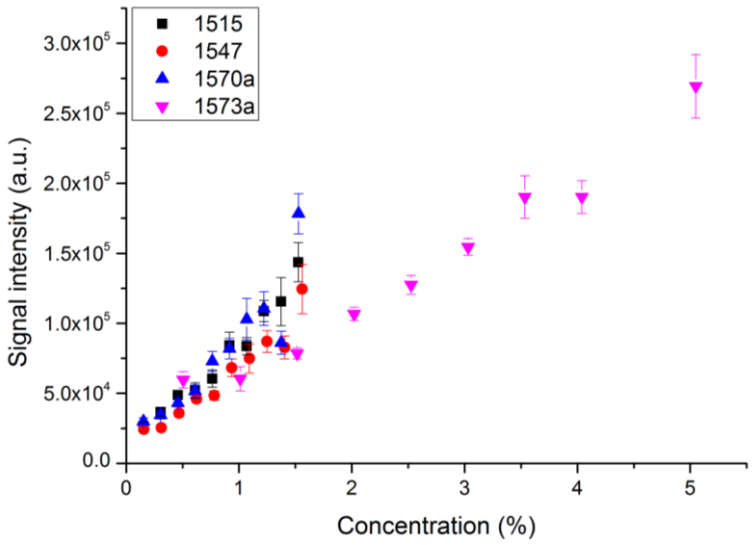

Fig. 4.11 Univariate calibration curve of Ca from four types of CRMs

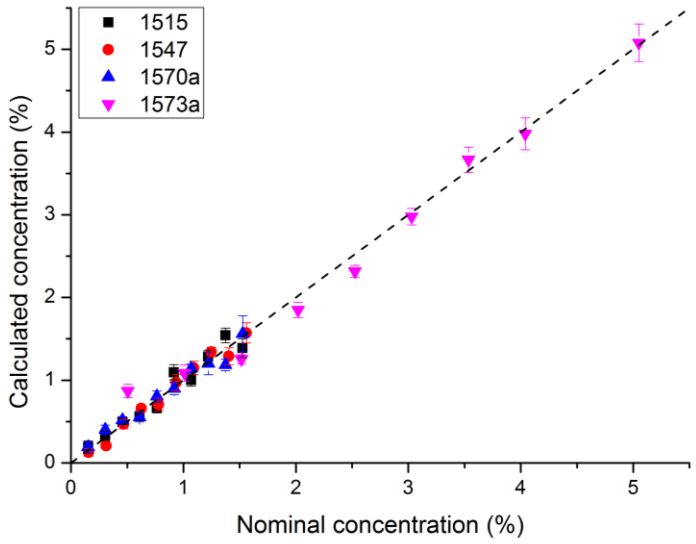

Fig. 4.12 Multivariate calibration of Ca from four types of CRMs

Linear regression model based on PLS (Partial Least Square) was developed to handle the matrix effect. Linear regression model applied to analysis that is extended to several variables is represented by Eq. (4.2).

$$Y = m_1 X_1 + m_2 X_2 + \cdots + m_n X_n + e \qquad \text{(mX : PC)} \qquad \text{- (4.2)}$$

PC is the acronym for principal component so PC 1 indicates most important variable and number of PC means how many variables were used. The accuracy of calculated concentration is different depending on the number of PC. In this study, 10 variables were considered. Fig. 4.12 shows the relation between nominal (actual) concentration and calculated concentration by multivariate calibration with all concentration of four types of CRMs which were regarded as the standard samples. By applying the multivariate method generated calculated concentration set in good agreement with the nominal concentration when compared to Fig. 4.11 that is univariate analysis.

Several arbitrarily chosen CRMs were regarded as the standard and unknown samples to ascertain how many types of CRMs should be considered for correction of matrix effects with high accuracy as shown Table 4.4. Fig. 4.13 shows the result when using 20, 40, 60, 80, 100% of NIST 1573a samples as the standard and 10, 30, 50, 70, 90% of the CRMs as unknown samples. The concentration of several unknown samples has large difference with nominal concentration. It is not possible to correct the matrix

effect sufficiently when standards are selected among a single CRM. Also there is greater error in some unknown samples than univariate analysis.

Table 4.4 Arbitrarily chosen CRMs : as the standard and unknown samples

Standard sample	Unknown sample 1	Unknown sample 2
20, 40, 60, 80, 100% of 1515 20, 40, 60, 80, 100% of 1547 20, 40, 60, 80, 100% of 1570a 20, 40, 60, 80, 100% of 1573a	10, 30, 50, 70, 90% of 1515 10, 30, 50, 70, 90% of 1547 10, 30, 50, 70, 90% of 1570a 10, 30, 50, 70, 90% of 1573a	10, 30, 50, 70, 90% of all the CRMs
20, 40, 60, 80, 100% of all the CRMs	10, 30, 50, 70, 90% of 1515 10, 30, 50, 70, 90% of 1547 10, 30, 50, 70, 90% of 1570a 10, 30, 50, 70, 90% of 1573a	10, 30, 50, 70, 90% of all the CRMs

Selected standard sample based on elemental concentration	Unknown sample
Group 1 : 1515-100%, 1547-20%, 1547-80%, 1570a-40%, 1573a-80% Group 2 : 1515-60%, 1547-100%, 1570a-20%, 1573a-60%, 1573a-100% Group 3 : 1515-20%, 1547-60%, 1570a-80%, 1573a-40%, 1573a-80% Group 4 : 1515-100%, 1547-20%, 1570a-60%, 1570a-100%, 1573a-100% Group 5 : 1515-80%, 1547-40%, 1547-80%, 1570a-100%, 1573a-20%	All the rest of samples

Figure 4.14 and 4.15 present the multivariate calibration of Ca when samples belonging to group 1 and 2 from Table 4.4 were regarded as the standard and the rest of samples were unknown sample, respectively. Each group consist of all kind of CRMs. Group 1 and 2 were chosen based on Al and Ca concentration, respectively. Calculated concentration is generally accurate except one sample in Fig. 4.14. On the other hand, most samples

have great difference between nominal and calculated concentration in Fig. 4.15. Therefore we confirmed the difficulty in estimation of accurate concentration when too few of samples were considered as standard even though many types of CRMs were used. We can conclude the multivariate analysis cannot completely overcome the matrix effect but it can greatly reduce matrix-match requirements between samples and standards by using standard samples of various type and concentration. Furthermore multivariate method can significantly decrease the error compared with univariate analysis.

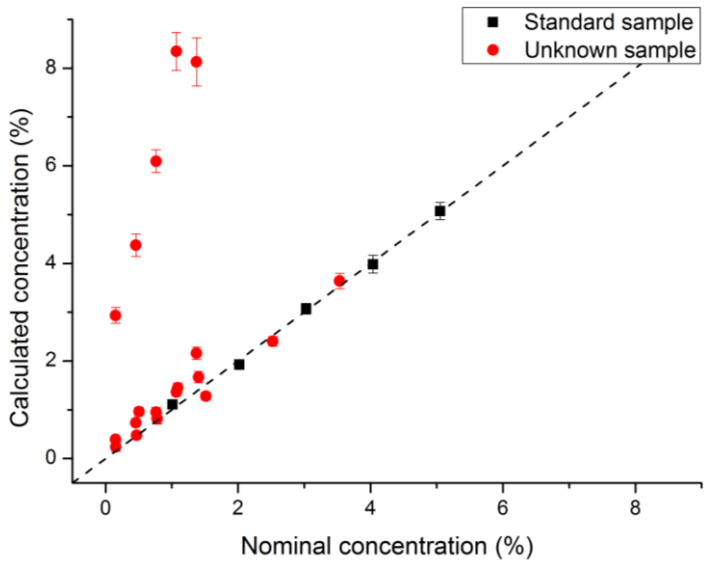

Fig. 4.13 Multivariate calibration of Ca

(20, 40, 60, 80, 100% of NIST 1573a were regarded as the standard and 10, 30, 50, 70, 90% of all the CRMs were unknown sample)

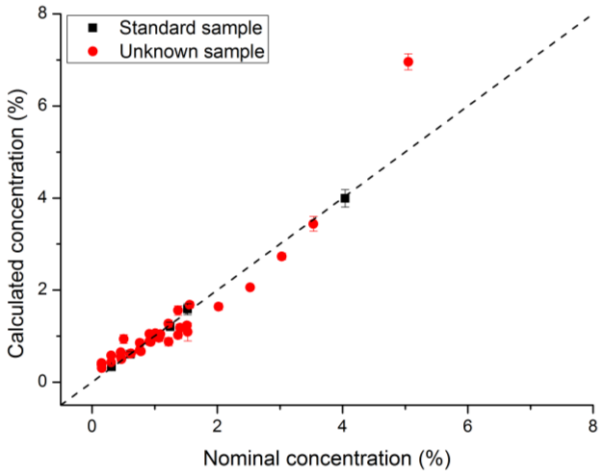

Fig. 4.14 Multivariate calibration of Ca

(samples belong to the group 1 from Table 4.4 were regarded as the standard and all the rest of samples were unknown sample)

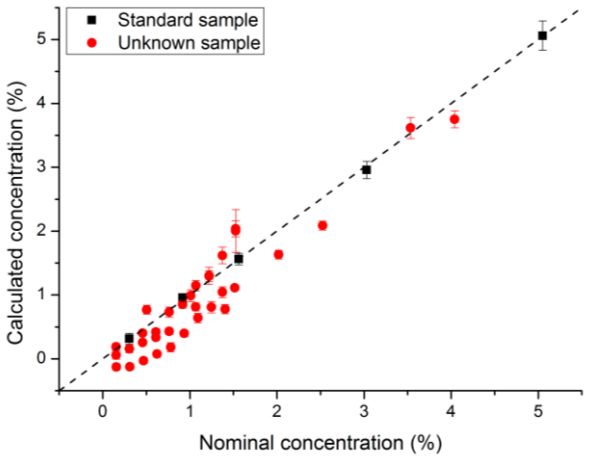

Fig. 4.15 Multivariate calibration of Ca

(samples belong to the group 2 from Table 4.4 were regarded as the standard and all the rest of samples were unknown sample)

CHAPTER 5

PLASMA CHARACTERISTICS BY ENVIRONMENTAL CONDITION [40]

5.1 Background and objective

The research considering real management circumstances by simulating a space environment is required for applying the LIBS technique into space mission. We built a database to understand the effect of LIBS signals toward the characteristics of samples and to predict the characteristics under the working circumstances that is changing through the application of low pressure condition.

The LIBS plasma characteristics are strongly dependent on the ambient pressure [41], while temperature is not dominant factor due to extremely higher temperature of the plasma (~ tens of thousands K) than ambient. In general, lower pressure causes a rapid expansion of the plasma volume, leading to a faster decay of the excited species' number density and shorter plasma lifetime. However it is known that the signal to noise ratio increases at low pressure due to lower continuum and background signal. Figure 3 from Ref. [42] compares LIBS spectra taken at atmospheric condition and at vacuum conditions ~10^{-6} torr. Though the intensity of the LIBS spectrum

taken at vacuum is less intense than the LIBS spectrum at atmospheric condition, it is clear that the LIBS spectrum at vacuum has higher resolution. In this study, we analyzed elemental lifetime of specific targets (Graphite, Ni, Cu, Sn, Al, Zn) staged within a vacuum chamber for analysis of the effect of surrounding pressure. The LIBS plasma peculiarity in the vicinity of 1 torr is identified and the possible cause of such interesting phenomena is given.

5.2 Experimental condition

The experimental apparatus is specified in Table 2.1. A Q-switched Nd:YAG laser which operates at 1064 nm with output pulse energy of 45 mJ is focused onto the sample surface inside of a vacuum chamber by a BK7 lens of 300 mm focal length. Single shot was applied to the experiment and it was repeated 5 times in each case.

To collect the plasma, 50 μm fiber optic cable (ME-OPT-8004) was used. The detector located at perpendicular direction to the sample. The gate width was 50 μs and gate delay was varied from 100 ns to determine dynamic changes in the elemental lifetime of the sample. The gain of ICCD was 150.

The samples used for the experiments are carbon (graphite), nickel, copper, tin, aluminum, and zinc. Although the targets are not standard materials, the purity of each target is above 95%. The targets were mounted on a XYZ stage inside of a vacuum chamber of 760 to 10^{-5} torr where a set of turbo and rotary pump is used to evacuate the chamber.

5.3 Effect of ambient pressure from the elemental lifetime perspective

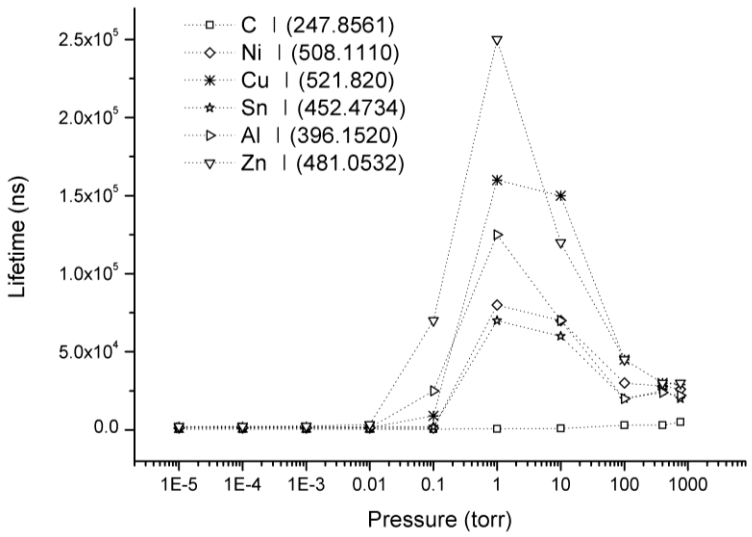

Fig. 5.1 Elemental lifetimes of neutral atoms (1 bar = 760 torr)

Figure 5.1 shows the elemental lifetime of neutral atoms according to the ambient pressure. Several representative emission lines of each element based on the NIST database [43] were analyzed. The elemental lifetime was measured within the range of detectable limit with more than 5 on the signal to noise ratio. As shown in the figure, the lifetime of carbon decreased for the entire range of pressure reduction. The remaining metal targets all showed peak lifetime at 1 torr and started to decrease with pressure reduction until all the elemental lifetimes reached constant value below 10^{-2} torr. This significant

increase of elemental lifetime at 1 torr except for the non-metallic (carbon) receives a closer look.

From the literature one finds that Yalcin and co-workers suggested a spectral enhancement of Al at 4 torr compared to atmospheric conditions at all gate delays [44]. The enhancement seen at 4 torr compared to atmosphere (760 torr) is likely a result of reduced plasma cooling at low pressures. Plasma cooling occurs when the ambient gas acts as cooling material for the hot vapor plasma [45]. Consequently, the lifetime of LIBS plasma created at 1 to 7 torr is much greater than that of a LIBS plasma created at an atmospheric condition. Another note from the literature is by Dreyer et al. where they observed a maximum spectral intensity of Ca, Mg, and Fe near 7 to 5 torr while decreasing intensity seen near 5 to 1 torr, suggesting a rapid decrease in electron density [46]. Also Cowpe et al. calculated electron number density from the Stark broadening of the 288.16 nm Si (I) emission line [36]. Figure 4 from Ref. [47] reveals that the step change in electron number density is evident, dropping by approximately an order of magnitude between ambient pressures of 7 and 0.7 torr. The electron number density is proportional to line broadening. Hence it is possible to get LIBS spectrum with higher resolution at low pressure condition compared with atmospheric pressure.

These literature findings indirectly suggest a ‘sweat spot’ in the low pressure zone near 1 torr. The present work attempts to clarify the noted feature in the vicinity of 1 torr where the maxima of elemental lifetimes exist

for metallic samples by considering the full range of ‘vacuum’ pressure.

5.3.1 Characteristics of lifetimes with pressure change

5.3.1.1 High vacuum, $10^{-5}<P<10^{-2}$ torr

The elemental lifetimes of LIBS plasma are not affected by the pressure change in this region as the extremely rapid plasma expansion results in a very short elemental lifetime of less than a microsecond. It is too short a time to be influenced by the cooling effect and to be reduced by the plasma shielding, i.e., the laser energy coupled to the surface decreases due to the absorption of the irradiated energy by the plasma [48]. Typically the optimum delay time for turning on the spectrometer is one or two microseconds after the plasma initiation at atmospheric pressure because of the strong continuum. Below 10^{-2} torr, however, spectra have to be detected at earlier times because LIBS plasma disappears before 1 μs. However the intensity of continuum and background signal also drops under this condition, making such LIBS detection still possible.

5.3.1.2 Medium vacuum, $10^{-2}< P<1$ torr

While the pressure is further lowered in the medium vacuum range, all of the elemental lifetimes declined for the pressure ranging from 1 to 10^{-2} torr. In general, the effects of plasma cooling and plasma shielding gradually decrease

with the decreasing pressure because there is not enough material to take up the heat. Besides, if the mean free path is too large, the small chance of collision makes generation of excitation and ionization difficult. For this reason, there are not enough excited atoms, ions, and electrons for collision with each other, and this causes the elemental lifetime to decrease, despite reducing the plasma cooling effect under this pressure condition.

5.3.1.3 Low vacuum, 1<P<760 torr

From 1 to 760 torr, most of the elemental lifetimes increase while carbon showed a decrease. As mentioned, the low pressure causes reduction in the plasma cooling and shielding effect. During a slow decrease in the plasma temperature, the atoms maintain their excited state for a prolonged period of time. Furthermore the small mean free path around 760 torr results in insufficient collision velocity for generation of strong atomic excitation. At a particular pressure state namely at 1 torr, optimal mean free path for atomic collision is allowed. Below 1 torr however, the mean free path is excessively large, and such the strong atomic excitation is very unlikely. These are just a few known complexities around low vacuum state, leading to the LIBS plasma peculiarity in the vicinity of 1 torr; namely, the maxima in elemental lifetimes of the samples (exception of a carbon) are reached. There is a strong evidence of proper pressure range that exists for optimal LIBS plasma spectroscopy in the low pressure conditions.

5.3.2 Analysis of elemental boiling point and electronegativity

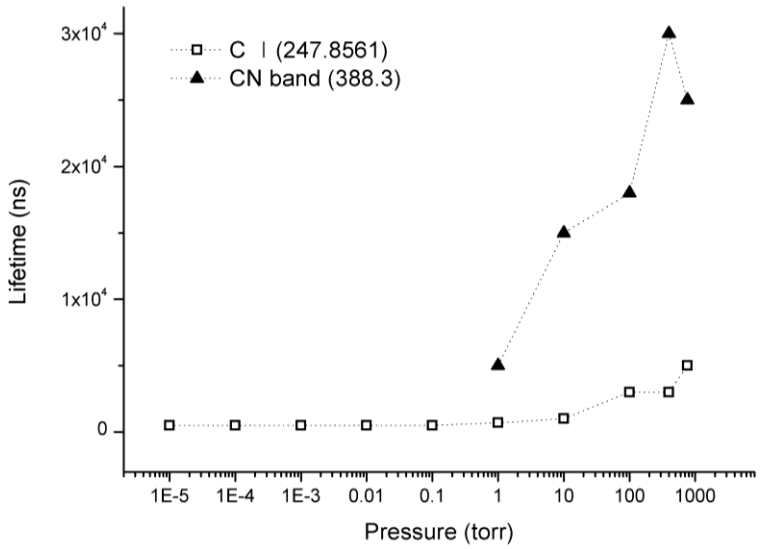

Fig. 5.2 Elemental lifetimes of neutral carbon atom and CN molecule

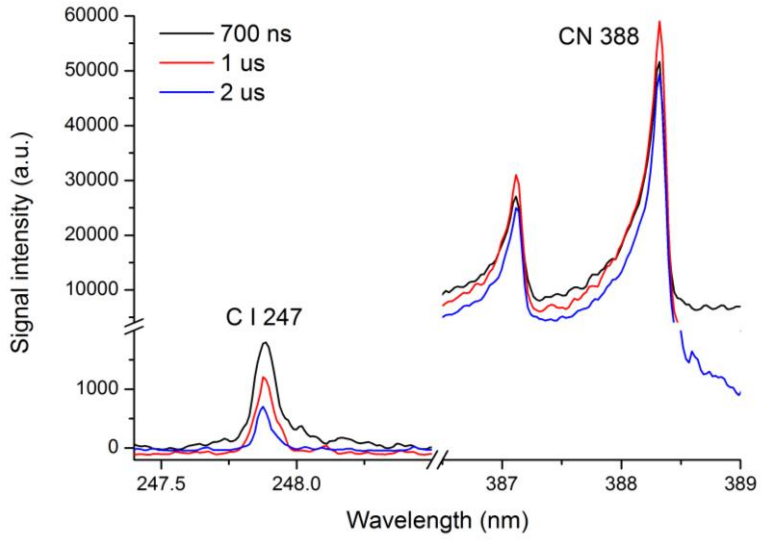

Fig. 5.3 Time-resolved spectra of neutral carbon and CN molecule

In the case of carbon, the plasma lifetime is reduced with decreasing pressure due to a rapid plasma expansion as shown Fig. 5.2. The difference of elemental lifetime characteristics results from the species' physical and chemical properties such as boiling point and electronegativity. The neutral carbon atom is disappeared quickly while carbon and nitrogen recombined (Fig. 5.3).

In the laser-material interaction at high irradiance, the sample surface temperature rises substantially above the vaporization temperature. The species are excited and plasma is generated. The plasma generation is associated with the boiling point and heat of vaporization of target material. Under low pressure conditions, the plasma cooling effect is weakened, and thus most of elemental lifetimes increased except for carbon. As shown in Table 5.1, carbon atom has high boiling point and heat of vaporization in atmospheric condition. This suggests that carbon is not affected by reducing the cooling effect because the carbon can condense at higher temperature. Zinc, however, has longest lifetime at 1 torr due to its low boiling point. Eq. (5.1) is the Clausius-Clapeyron equation [49] which gives the pressure and temperature relationship during vaporization, where R (= 8.3145 J mol^{-1} K^{-1}) and Δh are the gas constant and heat of vaporization. For a given state of vaporization at state 1 (P_1, T_1), a new state (P_2, T_2) along the curve is known. The boiling temperature of each element can be given from

$$T_2 = \frac{1}{\ln\left(\frac{P_1}{P_2}\right)\left(\frac{R}{\Delta h}\right) + \frac{1}{T_1}} \tag{5.1}$$

Table 5.1 Physicochemical properties of test samples [50]

Element	Atomic Radius [pm]	First ionization energy [kJ/mol]	Electro-negativity	Boiling point [K]	Heat of vaporization [kJ/mol]
C	67	1086.5	2.55	4300	715
Ni	149	737.1	1.91	3186	378
Cu	145	745.5	1.90	3200	300
Sn	145	708.6	1.96	2875	290
Al	118	577.5	1.61	2792	293
Zn	142	906.4	1.65	1180	119

Figure 5.4 shows plotted boiling temperatures of each element for various vapor pressures. One may infer a certain lower temperature than carbon curve where the effect of plasma cooling is insignificant. Below 3000 K at 1 torr for instance, the lifetime will be affected by reducing the plasma cooling as in all the metal samples. Then along this pressure dependent boiling curve, we can infer whether the specific element can be affected by reducing the cooling effect or not at full range of pressures.

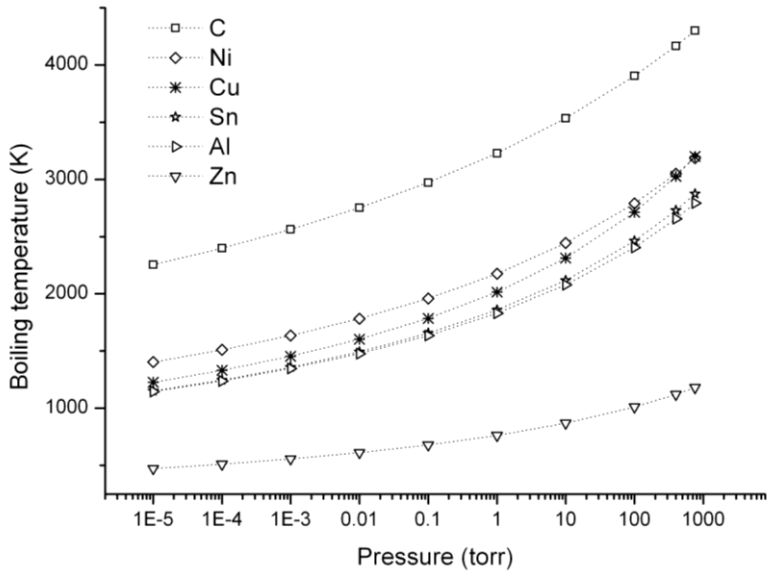

Fig. 5.4 Estimated boiling point of each element

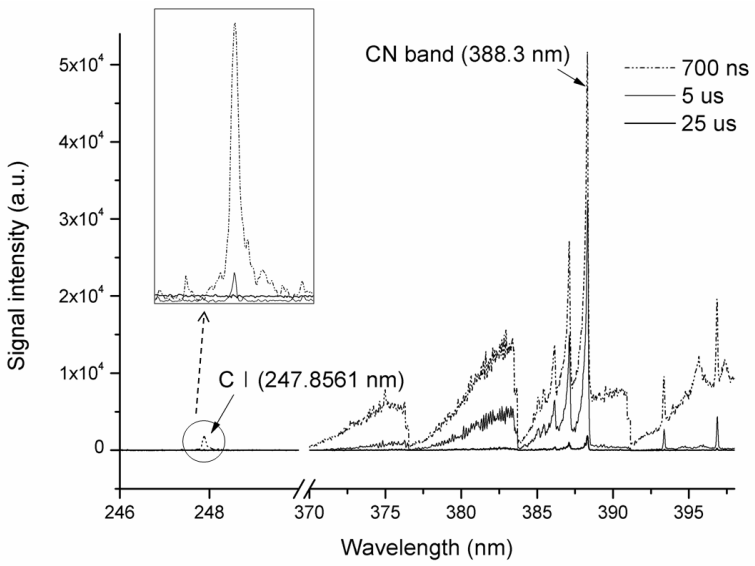

Fig. 5.5 LIBS spectra of CN band and neutral carbon atom from graphite sample according to gate delay at 760 torr

The emission line of carbon quickly disappeared with pressure decrease. At 760 torr, the neutral atom of carbon is detected until 5 μs. Shown in Fig. 5.2, above 1 torr, CN band is generated due to combination of carbon atom and nitrogen atom that exists in ambient atmosphere. The strongest CN band is appeared near 760 torr due to an abundance of nitrogen, and LIBS signal of a molecular band appeared because of the rotation and vibration of elements (Fig. 5.5). Table 5.1 shows carbon having the upper (or lower) limit of physicochemical properties amongst the tested samples. Both ionization energy and electronegativity increase with decreasing atomic radius. Electronegativity is a measure of the ability of an atom or molecule to attract pairs of electrons in the context of a chemical bond. Therefore despite the initial pressure of 760 torr, carbon atom line quickly disappears with pressure reduction because it combines easily with nitrogen atom; its large electronegativity being the main reason.

There remains a possibility that additional factors may affect the lifetime variation since laser-material interaction is a complex phenomenon that often complicates itself with the plasma shielding effect, signal intensity, wavelength range of emission line, and generation of molecules by reactivity of elements. Nevertheless, it is possible to infer elemental lifetimes from the physicochemical properties of test samples.

CHAPTER 6

DESIGN OF STAND-OFF DEVICE FOR SPACE EXPLORATION [51]

6.1 Background and object

In recent decade, there have been growing interest in applying stand-off LIBS at low pressure conditions in prior to space exploration [6-12]. More works of the stand-off LIBS were carried out at standard earth atmosphere. Palanco et al. used aluminum and titanium standard samples at 30~100 m distances at 760 torr to construct a field-deployable LIBS system [52]. An open-truss type telescope with the aperture of 16 inches was introduced and applied in such cases as detecting aerosols and explosive contaminated fingerprints and the studies of beam propagation [53-55]. Gottfried et al. used geomaterials and explosive samples at 20~30 m distance in 760 torr and carried out multivariate analyses to categorize each sample [56-59].

In this study stand-off detection was carried out to confirm the capability of LIBS system as a rover payload by considering the environmental condition. Also we built a compact LIBS prototype by combining commercial device to qualify the performance of compact LIBS system as a stand-off analyzer at low pressure condition.

6.2 Experimental condition

Nd:YAG laser operating at 1064 nm with the energy of 21.7~48.5 mJ/pulse. The laser beam is expanded by the 4 x beam expander for a higher collimation of the beam. It is focused on samples by fused silica lens with focal length of 5000 mm. The laser was focused on the sample surface and fired 5 shots at the same location.

The time delay of the spectrometer as used for pressure above 10 torr was 1 μs while it was 0.7 μs for below 1 torr tests. The gate width was 20 μs. The 200 μm fiber optic cable was connected to the spectrometer to collect the plasma emission. Fiber optic was located parallel to the sample surface.

As a stand-off detector of the emitting plasma light, we used a commercial refracting telescope (Kenko, 4") with the focal length of 500 mm. The telescope is located behind laser system, but is set in the higher position so that it is not interrupted by the laser system from detecting plasma light. Samples were placed with a distance of 5.7 m from the laser and 7.2 m from the detector at room temperature for a stand-off system.

Pressure inside the chamber varied from 10^{-2} torr to 760 torr. Samples were placed on the sample holder inside the vacuum chamber. The aluminum plate sample was used.

6.3 Stand-off detection

Aluminum peaks are measured with laser energies varied from 21.7~48.5 mJ/pulse, which is indicated in Fig. 6.1. Signals at 1 torr consistently showed the highest value amongst other pressure conditions regardless of the laser energy. Noticeably, even at 10^{-2} torr, Al I peaks are still detectable. When in stand-off condition, we only consider the plasma effect at low pressure inside the chamber. Therefore, air outside the chamber may cause errors or fluctuation of signals by affecting the laser beam propagation. Secondly, the focused region is elongated when using a focusing lens with a long focal length. This may cause variety in the focusing point, which is regarded as one reason for different plasma intensity particularly at 1~10 torr region where the error bar is the largest. Despite all these matters, signals at 10^{-2} torr can be detected at a low laser energy such as 21.7 mJ/pulse.

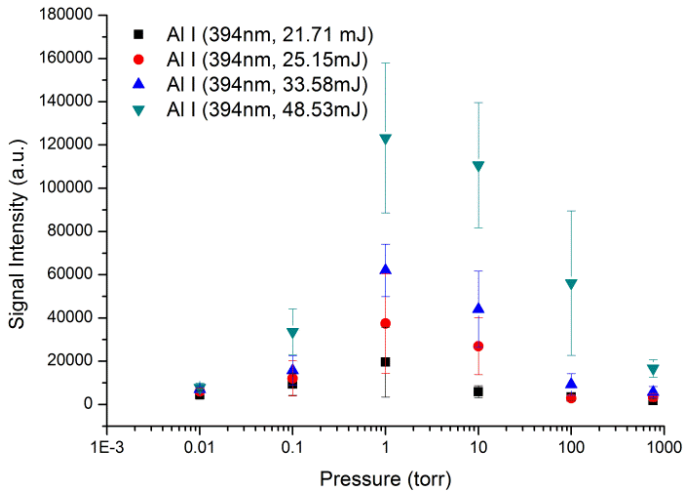

Fig. 6.1 Signal intensity of Al I 394.40 nm with different laser energy

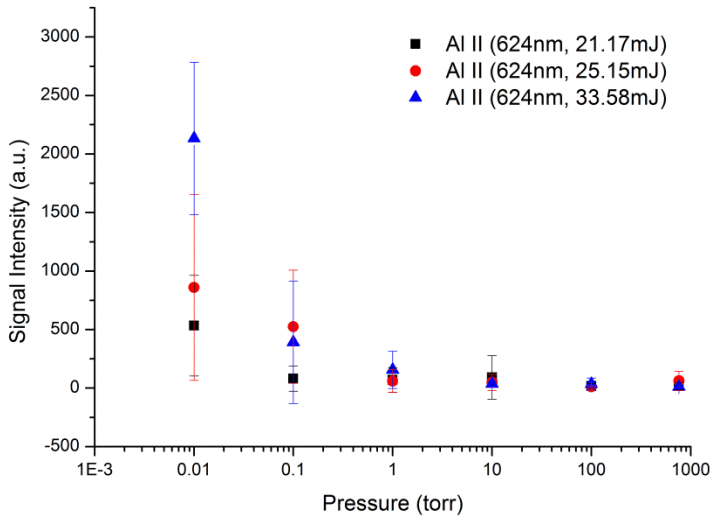

Fig. 6.2 Signal intensity of Al II 624.34 nm with different laser energy

The ionized aluminum peak in Fig. 6.2 is analyzed by using varying laser energies and pressures. Al II peak (624.34 nm) begins to appear below 1 torr. The reason why detection of ionized atoms at low pressure can be easier is related to the atomic reaction. When the atom is excited by the laser ablation, electrons are released and the atom is ionized. After the ionization process, electrons are attached through the collision and interaction between atoms. However, the low pressure condition delays this atomic collision and interaction process because of low electron number density, which provides easier detection of ionized peaks at low pressure. Also, the plasma shielding effect diminishes when pressure is low. It is almost negligible when in low pressure condition, because plasma expands quickly at low pressure. For both reasons, the ionized peaks are easier to be detected. It is very encouraging that

the Al II peak is shown with noticeable intensity at 10^{-2} torr suggesting that the stand-off LIBS detection in lunar condition is quite feasible.

6.4 Design of portable stand-off device

We configured compact and lightweight stand-off LIBS system namely SNU-prototype equipped with commercial instruments to study its feasibility at various pressure conditions prior to planetary mission planned in future. System requirements are shown in Table 6.1.

Table 6.1 System requirements

Device	Requirements
Laser	- Energy ~ 30 mJ - Wavelength : 1064 nm - Weight < 1 kg (expect power unit) - Volume < pi 60 mm, length 220 mm
Spectrometer	- Spectral range : 240-800 nm - Weight < 5 kg
Telescope	- Weight < 2.5 kg - Volume < pi 120 mm, length 150 mm

We have assembled SNU-prototype with commercial instruments with total mass of 5.5 kg. A 1064 Nd:YAG laser (Quantel, Ultra 50) with maximum pulse energy of about 69 mJ and pulse duration of 7 ns is selected. The laser beam passes through beam expander and fused silica plano-convex lens of focal length 500 mm located at the same axis of laser. Plasma is captured by

commercial 3.5 inch aperture Maksutov-Cassegrain telescope (Celestron C90), and its emission signal is introduced to a CCD detector (HR2000+CG). Spectrometer is covering a wavelength range of 200~1100 nm.

Figure 6.3 shows the compact LIBS system and comparison with ChemCam.

Component	SNU-LIBS (Dimension, mm)	ChemCam (Dimension, mm)	SNU-LIBS (Weight, kg)	ChemCam (Weight, kg)
Telescope	90 x 310 (D x L)	110 x 130 (D x L)	2.3	N/A
Laser	51 x 170 x 76 (H x L x W)	60 x 220 (D x L)	0.9	0.6
Spectrometer	45 x 149 x 105 (H x L x W)	120 x 120 x 100 (H x L x W)	0.6	N/A
Overall	200 x 350 x 150 (H x L x W)	166 x 377 x 211 (H x L x W)	5.5	5.62

Fig. 6.3 Compact LIBS system

CHAPTER 7

SIGNAL ENHANCEMENT AT LOW PRESSURE [60,61]

7.1 Background and object

Studies on laser induced plasma detection in low pressure condition have been performed for understanding the plasma characteristics that is sensitive to the ambient pressure [40-41,62-63]. It was reported that signal detection is effective at 1 to 10 torr due to a reduced plasma shielding effect and the existence of optimum mean free path at such pressure [40,44-46]. In a vacuum condition however, rapidly expanding and vanishing plasma causes its emission detection extremely difficult.

Several spatial confinement methods for enhancing the signal intensity of plasma emission have been reported in the literature. Shen et al. confined the plasma using two parallel walls and the cylindrical pipe of varying diameters [63], and showed that the cylindrical pipe is more effective than the parallel walls. The cylindrical pipe showed an enhancement in the signal due to the confined shock reflections that effectively reheated the plasma and strengthed the signal intensity. Guo et al. used a hemispherical cavity [64] for uniformly compressing the plasma within the cavity and studied the combined effects of

spatial confinement and dual-pulse irradiation [65]. Popov et al. used a small cylindrical chamber with polished brass walls (4 mm in diameter and 4 mm in height) to confine the plasma [66], which resulted in the improvement in both signal intensity and the limit of detection (LOD). Ding et al. investigated the plasma confinement effect by the reflected shockwave using metal disks with 2 mm hole in its center [67]. The reflected shock wave allowed the secondary enhancement of the signal intensity from CN molecules. Tao et al. performed a numerical analysis of the confinement effect using the microhole in Ar atmosphere and suggested that the plasma temperature, pressure, and thrust are enhanced due to the pressure wave reflections by the presence of a sidewall [68]. Zeng and Mao studied the effect of cavity with various aspect ratios in fused silica samples [69-70]. The plasma temperature and electron number density were at maximum when using the largest aspect ratio. Hou et al. improved both pulse to pulse signal repeatability and signal intensity by combination of cylindrical confinement and spark discharge [71]. They reported on the enhancements of spectral line intensity and the reduction of shot-to-shot fluctuation using the plasma image. Corsi et al. drilled craters of different depths on a copper sample to create cavity for the signal enhancement [72]. Hao et al. used ring magnet to spatially and magnetically confine the plasma [73]. They reported the enhancement of temperature and electron density of V and Mn. Li et al. performed numerical analysis using molecular dynamic simulation to investigate the temperature increase by

shock wave confinement [74]. The temperature, pressure, and number density increase were observed by the presence of shock reflections.

In all previous plasma confinement attempts, the key concept was to maximize the strength of the secondary pressure waves or the reflecting shock waves from confining the walls at an atmospheric pressure (760 torr). In doing so, a reheating of the plasma by shock reflection within the confinement was proven useful in the signal enhancement. With the lowered ambient pressure as in the present work, shock strength can no longer be sustained and thus an alternative approach is required for further enhancing the signal strength. A confining window above the sample is placed for successfully preventing rapid plasma extinction and increasing the electron density at low pressure conditions as the direction of plasma expansion is being controlled. Various neutral atoms and molecules are considered and five different window materials of varying transmittance at 1064 nm are used in order to validate the proposed confinement method. The present study provides an important guideline as to how to strengthen the weak signal intensity of the plasma at low pressure conditions by using a plasma direction controlled confinement scheme. Also confinement scheme can be applied for lander payload as a shape of arm of rover to enhance the LIBS performance.

7.2 Experimental condition

The experimental apparatus is specified in Table 2.1. Pulse energy of 34.3 mJ is focused onto the surface of a sample placed inside of a vacuum chamber. The laser beam is perpendicular to a surface of the sample. The emission from the plasma was detected through the side-view window. To collect the plasma, uncoated quartz lens of 100 mm focal length was used. The gate delay is varied from 0.1 to 0.5 μs while gate width is set to 1.05 ms. Sample is mounted on a XYZ stage inside a chamber, de-pressurized from 760 to 0.1 torr.

The confining window of 1 mm thickness and 12.7 mm diameter was placed at 2 mm above a sample by two confining walls that effectively guide the plasma to freely expand in a single direction (Fig. 7.1 and 7.2). When a shockwave strikes the confining material, part of the energy of the shockwave is transmitted to the material, and the remainder of the energy gives rise to forming the reflected shockwaves that travel back towards the sample. The impedance is the product of wave velocity and density, representing the measure of opposition. With a higher impedance mismatch between two contacting materials, reflection of shock wave is likely, as opposed to transmission. In our setup, this reflection of shockwave is no longer utilized as such a reflection would not occur at the near vacuum condition. Hence carefully selected confining material for this setup was acrylic which has a low impedance. Potentially decreasing electron density at low pressure

condition is effectively handled by the present confinement set up.

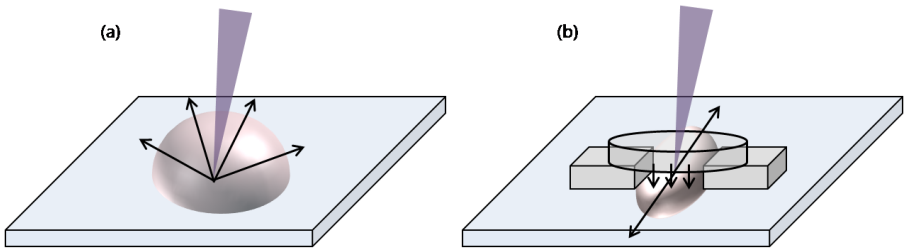

Fig. 7.1 Direction of plasma expansion at low pressure

(a) Free expanded plasma, (b) Confined plasma

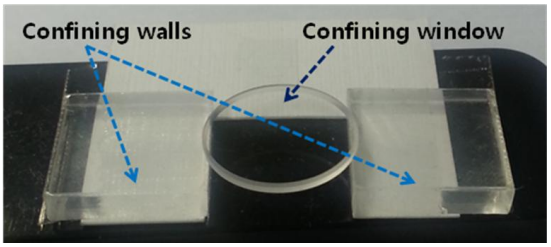

Fig. 7.2 Setup of confining window and walls

Various metal samples such as Al alloy, Brass, Ni, Ti, Sn and Graphite were considered for finding their elemental characteristics, and the USGS certified reference material was selected for the detection of Sulfur. The laser beam was focused on the sample surface and fired on 3 locations with 5 shots for each location. The confining window was replaced after irradiation of 5 pulses to prevent deposition of ablated particles on the surface of window. Acrylic window for its good price can be replaced for such repeated experiments. For

the optimal window material selection, Acrylic, BK7, Sapphire, Fused silica, and Magnesium fluoride were considered with their inherent transmittance to a 1064 nm beam.

7.3 Effective energy delivery at low pressure

Figure 7.3 shows the signal intensities of Al I and Al III emission line affected by the thickness of the acrylic window. The signal intensity becomes markedly lower at 760 torr as thickness of the window becomes larger, as shown in Fig. 7.3(a). The laser energy loss is higher when thickness of the acrylic window is large based on the Lambert-Beer law which proves the linearity between the absorbance and the thickness of the absorbing layer. In other words, smaller laser energy reaches the sample surface when using the acrylic window of 5 mm thickness, since thicker the window the more laser energy is absorbed. This energy loss can be minimized by using the window with its high transparency. Figure 7.3 (b) and (c) involves three different window thicknesses at 1 torr and suggests that optimum detection scheme as oppose to generation of strong plasma is more important in the low pressure LIBS study. Therefore the ablated mass confinement method as described here fulfills that purpose of a highly reliable LIBS detection.

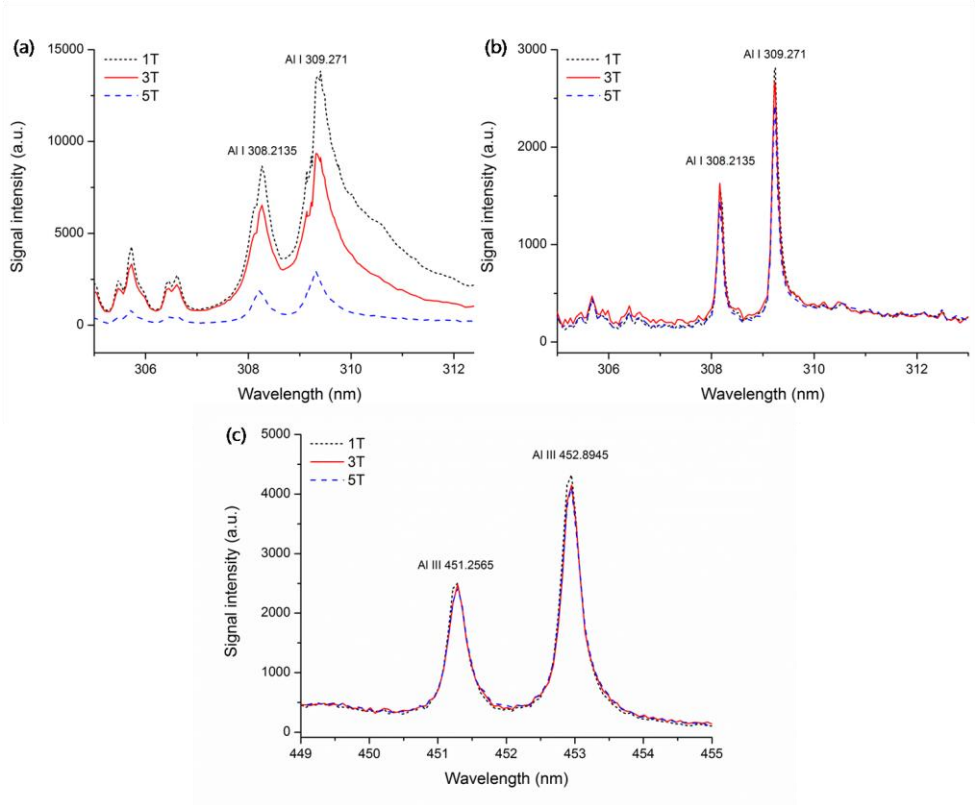

Fig. 7.3 spectra according to thickness of acrylic window

(a) Al I at 760 torr, (b) Al I at 1 torr, (c) Al III at 1 torr

The change of the signal intensity of Al I 309.271 nm emission line for varying laser energy at 760 and 1 torr is shown in Fig. 7.4. Plasma detection at atmospheric pressure is effective with a higher laser energy above 20 mJ/pulse. For the energy below 20 mJ/pulse, the SNR becomes low until no further signal is detected at 3.664 mJ. At 1 torr, the signal intensity is lower when using a high laser energy (i.e. above 20 mJ/pulse) compared to the

atmospheric pressure condition. However, in this case, the signal intensity slowly decreases when the laser energy drops. The order of signal intensity finally reverses at energy below 20 mJ/pulse where the 760 torr signal is below the 1 torr result.

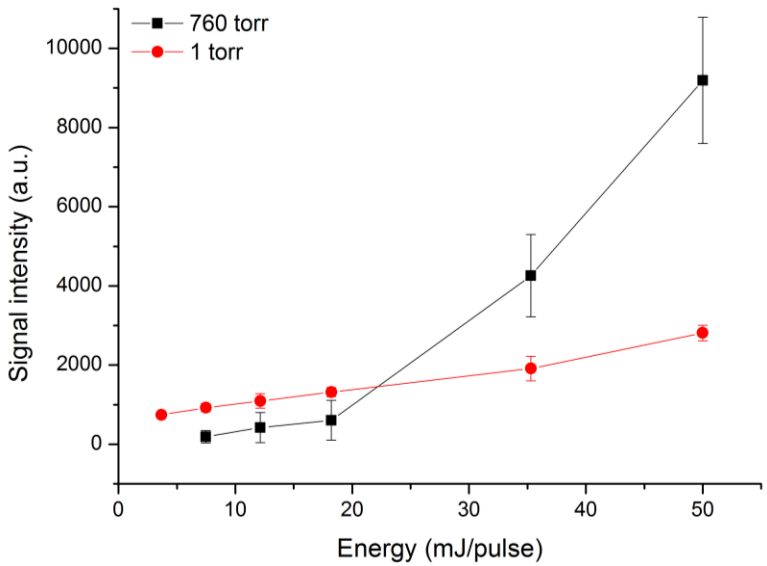

Fig. 7.4 Signal intensity of Al I 309.271 emission line at 760 and 1 torr plotted as a function of laser energy

The effective plasma generation depends on the energy threshold and the ambient condition. At high pressure, the plasma shielding effect and dust may interrupt a free plasma generation as in the case of a low pressure condition, but the rapid plasma expansion at low pressure makes it difficult for detection.

In this research, aluminum signal is successfully detected below 1 torr using a small energy of 3.664 mJ/pulse at a low pressure condition and by using the plasma confinement method, overcoming the well-known challenges of a low pressure plasma detection. This is why the present confinement scheme is a suitable technique when used with a low pressure scheme. In addition, the error is lower at 1 torr, suggesting that a high sensitivity detection is achievable at this combined method of low energy and low pressure as illustrated in the present investigation.

7.4 Low pressure effect

Figure 7.5 shows the confinement effect of neutral atoms at 1 torr. Unconf and Conf represent the unconfinement (free expansion) and confinement cases, respectively. By confinement, signal intensity of all the elements improved at least 1.5 times compared to a free expansion using a single laser pulse. The plasma persistence time of carbon, nickel, and tin which have shorter persistence time than aluminum, copper, and zinc in our earlier results in Fig 1 of [40] is also increased. The electron density of plasma rapidly decreases without confinement while the confinement allows the plasma to merge along a single direction of detection. The resulting plasma has high electron density and the extended persistence time. Significantly increased amount of ions, atoms, and molecules is collected along the controlled direction of the plasma.

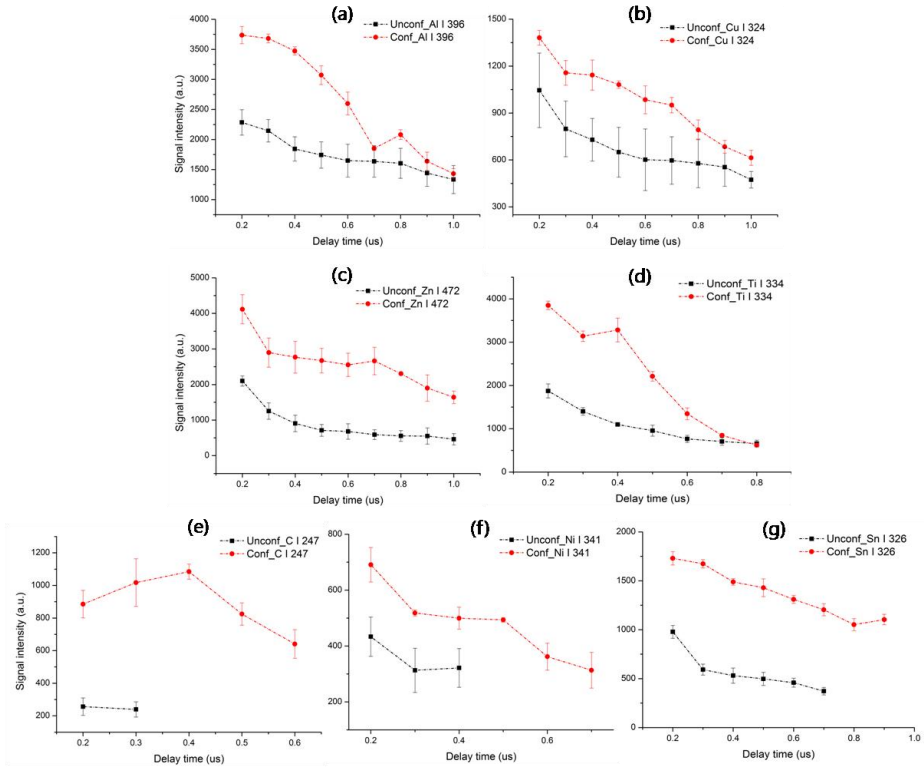

Fig. 7.5 Effect of ablated massplasma confinement of the neutral atoms at 1 torr (a) Al I 396 nm, (b) Cu I 324 nm, (c) Zn I 472 nm, (d) Ti I 334 nm, (e) C I 247 nm, (f) Ni I 341 nm, (g) Sn I 326 nm

Table 7.1 is confined/unconfined signal ratio of neutral atom using a single laser pulse. In our setup, energy loss occurs while the beam is transmitted through the acrylic window of 92% transmittance at 1064 nm. Thus signal intensity decreases at normal pressure where the confinement is not critical for generating a strong plasma for detection. The signal intensities of carbon and aluminum at 760 torr by confinement are greatly declined. These two

elements can recombine with nitrogen and oxygen which are included in the air. When confinement is applied, the increase of electron density in limited space causes rapid recombination of excited atoms, and thus atomic signals have low intensity and short persistence time. The persistence time of neutral carbon is shorter than aluminum because carbon has a large electronegativity which is a measure of tendency for either atoms or functional group to attract the electrons towards themselves. Hence carbon has weak signal intensity and small persistence time due to rapid extinction by recombination in the presence of nitrogen.

Table 7.1 Confined/unconfined signal ratio of neutral atoms using a single laser pulse

Element	760 torr	100 torr	10 torr	1 torr	0.1 torr
C	0.37	0.39	0.69	4.25	Detected if confined only
Al	0.54	0.96	1.18	1.72	1.95
Cu	0.87	0.94	1.07	1.45	1.54
Zn	0.92	1.03	2.10	2.31	2.53
Ni	0.96	1.62	2.02	1.66	Detected if confined only
Sn	0.93	0.73	1.65	2.83	2.24
Ti	0.95	0.91	1.48	2.24	2.40

However confinement effect becomes clear at pressure below 100 torr where the signal intensity increases at least 1.5 times. The signal intensity can

further increase by accumulation of the several laser pulses. Also, one notes that carbon and nickel are only detectable at 0.1 torr with confinement.

Table 7.2 shows the electron density of Al I (396 nm) at 2 μs delay time. Although the signal intensity of neutral aluminum by confinement is greatly decreased at 760 torr, the electron density is increased. The confining plasma expansion in a limited space using a confining window causes the increase in both electron density and persistence time. Furthermore, more ions, atoms, and molecules reach the detector along the controlled path in the proposed confinement set up. The plasma expansion occurs at the early times right after the plasma initiation, and thus the confinement effect is also started immediately.

Table 7.2 Electron density of Al I (396 nm) at 2 μs delay time

Pressure [torr]	Electron density [10^{18} cm^{-3}]	
	Unconfined	Confined
760	0.138984	0.148332
1	0.059963	0.091889

Figure 7.6 shows the change of molecular band signal from a graphite sample at atmospheric pressure. When confinement is used, the increase of electron density within the limited space causes rapid recombination of excited atoms. The rapid recombination causes decrease of atomic emission. Instead, strong molecular signal appears by the recombination of atoms as shown Fig. 7.6 CN molecule is generated by recombining the ablated carbon

from the sample and the nitrogen of an air. Air-combined molecules have remarkably small persistence time by confinement because supplied air is insufficient for generating a strong molecular signal in the limited space.

In contrast to air-combined molecules, C_2 molecular band that is formed from the product material of the sample showed strong intensity and longer persistence time with the confinement applied. The electronegativity that defines the tendency of an atom to attract electrons towards itself, of nitrogen is higher than that of carbon, and thus the C-N bond is generated more easily than the C-C bond. This explains why the C_2 band signal from the free expansion has a weak intensity. Whereas C_2 band formation occurs rather strongly while the expansion of carbon atom towards an air is disrupted by the presence of an acrylic window in our system.

The signal increment by confinement of neutral carbon at low pressure in Table 7.1 supports the result of the molecular signals. The signal of neutral carbon with confinement decreases at high pressure conditions above 1 torr due to its recombination with nitrogen. Air becomes thinner as the pressure is lowered, thus the confinement allows for signal enhancement at pressure below 1 torr.

We have checked the molecular signals at such low pressures. Signals of CN and C_2 molecular band decrease as pressure is decreased and disappear when below 10 torr. Therefore signal enhancement of neutral carbon by confinement starts to appear at 1 torr as in Table 7.1.

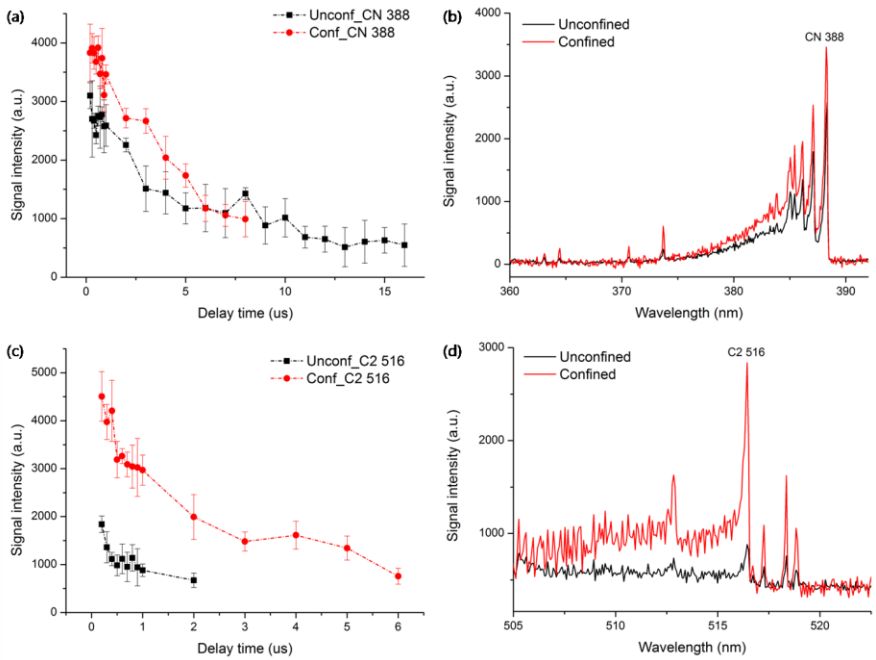

Fig. 7.6 Effect of ablated mass confinement of the molecular bands at atmospheric pressure (a), (b) CN 388 nm, (c), (d) C_2 516 nm

The highly ionized atom was also investigated. The doubly ionized carbon atom is not detected at 760 torr as shown Fig 7.7. C III emission line appeared at 1 torr when no confinement is applied. The low pressure condition allowed for a reduction in the plasma shielding, resulting in lesser obstruction along the beam path. Besides, highly ionized atoms are also not readily combined with electrons. In the confinement case, the signal intensity (or signal to noise ratio) increase is quite evident. A rapid extinction of plasma is delayed as the plasma is effectively isolated within a 2 mm confinement spacing.

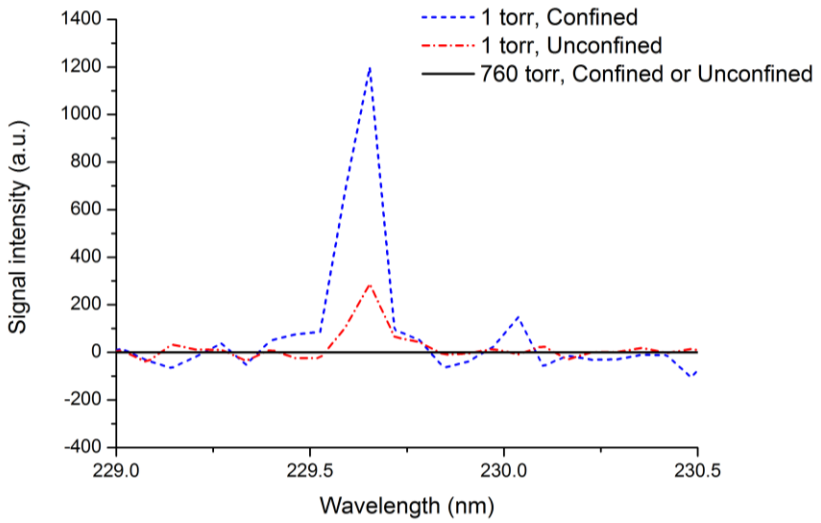

Fig. 7.7 Spectra of doubly ionized carbon atom

7.4 Hard-to-detect element – Sulfur detection

The present confinement scheme may facilitate the detection of minor elements and those hard-do-detect elements such as sulfur, chlorine, and phosphorous. Strong emission lines of these elements are reported to occur either in the UV or near IR region, and the excited atoms readily react with atmospheric oxygen. Besides, these elements have high ionization energy, and thus detection of S, Cl, P has known quite challenging. In the past, researchers attempted to detect such elements by using the double pulses at high laser energy [75] or the buffer gases [76] and low pressure conditions [77] for potential detection.

Here we provide a result of sulfur detection by using a single laser pulse at low laser energy combined with the present confinement method. The target sample is MASS-1 which is a USGS certified reference material that contains 27% of sulfur, and the accumulation of five spectra are used for generating the result. Figure 7.8 shows sulfur spectra with respect to pressure. Without confinement, neutral sulfur peaks appeared with a very low signal to noise ratio at the atmospheric pressure, while the peak is quite non-distinguishable at the lowered pressures. Most of neutral atoms are easily detectable at atmospheric pressure with a CCD detector which has a long gate width as shown in Table 7.1. We find that the low pressure condition allows for an effective detection of certain element namely the sulfur which quickly recombines with the oxygen in air. Consequently the signal to noise ratio is enhanced. To estimate SNR of S I 921 nm, background subtraction was performed using the Aurora software (Applied Spectra Inc.). Two ratios of the peaks namely 921 nm and 915 nm were used for SNR. For 760 torr unconfined case, SNR was 3.34, and for 10 torr confined case, SNR was 20.15. Thus the present work is also effective in terms of utilizing the pressure conditions for detecting those hard-to-detect elements of a wide interest.

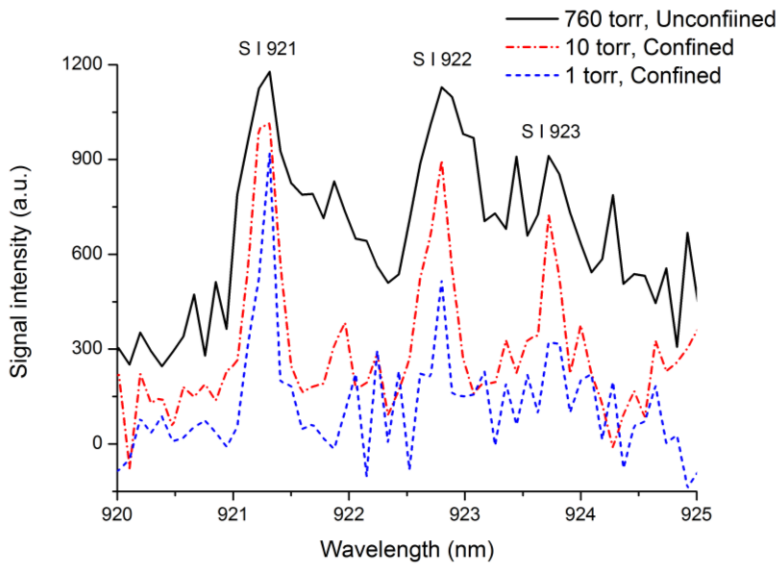

Fig. 7.8 LIBS Spectra of neutral sulfur atom

7.6 Effect of a confining window material

Up to now, we used acrylic window which has 92% of transmittance at 1064 nm wavelength. To compare the effect of window materials, five different materials were considered that include Acrylic, BK7, Sapphire, Fused silica, and Magnesium flouride. The transmittance of each material is summarized in Table 7.3.

Table 7.3 Transmittance of window material at 1064 nm

	Acrylic	BK7	Sapphire	Fused silica	MgF_2
Material Transmittance (%)	92	92	83	98	98

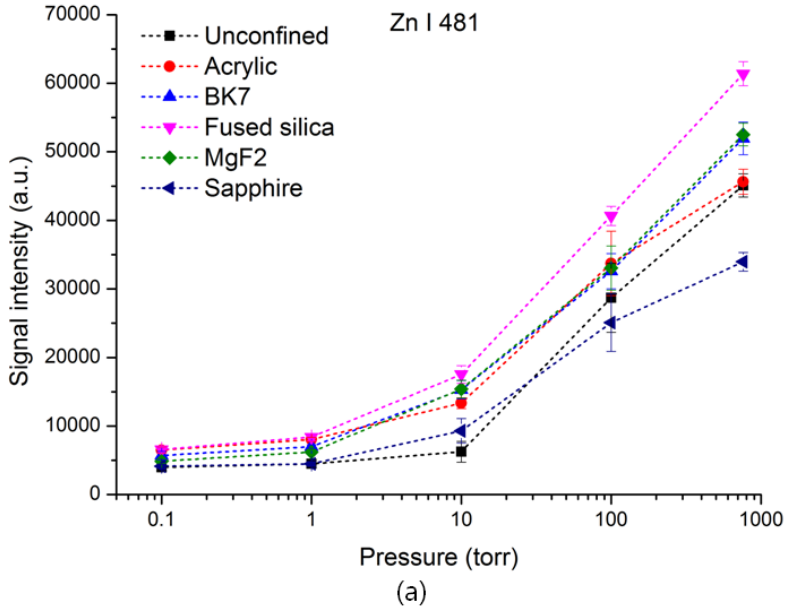

Fig. 7.9 Effect of confining window material (a) Zn 481 nm, (b) Cu 521 nm

Fig. 7.9 shows signal intensities with respect to pressure for various materials. For acrylic window and sapphire window, the signal enhancement was noticeable only if the pressure is lowered below 100 torr due to energy losses. For all other window materials of higher transmittance, the signal enhancement was observed at all pressure range. Despite the low transmittance of only 83%, we performed the signal enhancement at low pressure using sapphire. The confinement effect using sapphire was visible at pressure below 1 torr only. The results suggest the optimal window materials for the present confinement scheme aimed at low pressure detection.

CHAPTER 8

CONCLUSION

In this study, we have specified the LIBS system requirements for space exploration. By using double pulse, signal intensity is remarkably increased when compared to the single pulse case. Also by applying optimum angles of both the sample and the detector, a significant signal enhancement of each element is proven possible. Furthermore, proper wavelength of Nd:YAG laser for space mission was fundamental (1064 nm).

A quantitative LIBS analysis was applied to handle the matrix effect. The 21 powdered CRM samples from NIST and USGS were chosen from agricultural materials, foods, clays, soils and sediments, steelmaking alloys, and geochemical reference materials based on the samples' basic constituents. The PCA method was applied to categorize the samples with similar characteristics. The obtained calibration curves exhibit significant improvement to their curve accuracy through the chemometrics procedure.

Also elemental lifetimes of six different samples were investigated in a low-pressure chamber which has the pressure range of 760 to 10^{-5} torr. The peculiarity at 1 torr is observed for all samples except for carbon whose lifetime showed uniform decrease with lowering of the pressure due to a rapid plasma expansion. High boiling point and electronegativity are analyzed for

explanation of the present observation of carbon. For the samples other than carbon, lifetimes increased during the prescribed pressure decline from 760 to 1 torr, and then decreased with continued pressure lowering from 1 to 10^{-2} torr. Below 10^{-2} torr, the lifetime of LIBS plasma was no longer affected by the pressure change. Possible reasons why maxima in the LIBS plasma lifetime for each sample occurred at 1 torr are believed to come from the plasma cooling and shielding effect, the plasma expansion, and the variation in the mean free paths for the surrounding pressure.

Aluminum emission at stand-off distance reached a maximum at 1 torr and signals at 0.1 torr and 0.01 torr were quite identifiable. Stand-off LIBS at pressure below 1 torr is proven quite feasible suggesting its use during lunar exploration mission. The compact LIBS system was assembled successfully to have compact and lightweight.

And we suggested the confinement scheme to improve the low pressure detection. The confinement configuration consists of two end walls capped with a transparent window that prevents rapid plasma dissipation while controlling the direction of the plasma expansion towards the detector. The enhancement factors of 1.5 to 4.2 in all elemental signals were obtained by the confinement at the low pressure conditions. The signal intensity and signal to noise ratio of highly ionized atoms which appear only at low pressure were also greatly improved by the present detection scheme. This work suggests that the LIBS has clear potential as a space exploration tool.

REFERENCES

[1] N. Hasebe, N. Yamashita, O. Okudaira, S. Kobayashi, H. Yamamoto, T. Ishizaki, K. Hirano, K. Sakurai, T. Miyachi, M. Miyajima, M. Fujii, M.-N. Kobayashi, T. Takashima, E. Shibamura, O. Gasnault, S. Maurice, C. d'Uston, R. Reedy, and M. Grande, "The high precision gamma-ray spectrometer for lunar polar orbiter SELENE," Adv. Space Res., Vol. 42, 2, pp. 323–330, 2008.

[2] R. Rieder, T. Economou, H. Wänke, A. Turkevich, J. Crisp, J. Brückner, G. Dreibus, and H. Y. McSween, Jr., "The chemical composition of Martian soil and rocks returned by the mobile alpha proton X-ray spectrometer : preliminary results from the X-ray mode," Science, Vol. 278, 5344, pp. 1771–1774, 1997.

[3] M. L. Pascu, "Laser physics elements to consider for low level laser therapy," Laser Therapy, Vol. 13, pp. 114-125, 2001.

[4] http://www.industrial-lasers.com/articles/print/volume-27/issue-03/features/fiber-lasers-boost-medical-device-production.html

[5] A.B. Gojani, J.J. Yoh, J.H. Yoo, "Extended measurement of crater depths for aluminum and copper at high irradiances by nanosecond visible laser pulses," Applied Surface Science, Vol. 255, pp. 2777-2781, 2008.

[6] F. Colao, V. Lazic, R. Fantoni, A. Paolini, "LIBS application for analyses of Martian crust analogues: search for the optimal experimental parameters in air and CO_2 atmosphere," Appl. Phys. A, Vol. 79, pp. 143-152, 2004.

[7] S.M. Clegg, E. Sklute, M.D. Dyar, J.E. Barefield, R.C. Wiens, "Multivariate analysis of remote laser-induced breakdown spectroscopy spectra using partial least squares, principal component analysis, and

related techniques," Spectrochimica Acta Part B Vol. 64, 1, pp. 79-88, 2009.

[8] J.B. Sirven, B. Sallé, P. Mauchien, J.L. Lacour, S. Maurice, G. Manhès, "Feasibility study of rock identification at the surface of Mars by remote laser-induced breakdown spectroscopy and three chemometric methods," J. Anal. At. Spectrom., Vol. 22, pp. 1437-1568, 2007.

[9] B. Salle, J. Lacour, E. Vors, P. Fichet, S. Maurice, D.A. Cremers, R.C. Wiens, "Laser-induced breakdown spectroscopy for Mars surface analysis: capabilities at stand-off distances and detection of chlorine and sulfur elements," Spectrochim. Acta B. Vol. 59, pp. 1413-1422, 2004.

[10] B. Salle, D.A. Cremers, S. Maurice, R.C. Wiens, P. Fichet, "Evaluation of a compact spectrograph for in-situ and stand-off Laser-Induced Breakdown Spectroscopy analyses of geological samples on Mars missions," Spectrochim. Acta B. Vol. 60, pp 805-815, 2005.

[11] J.R. Thompson, R.C. Wiens, J.E. Barefield, D.T. Vaniman, H.E. Newsom, S.M. Clegg, "Remote laser-induced breakdown spectroscopy analyses of Dar al Gani 476 and Zagami Martian meteorites," J. Geophys. Res. Vol. 111(5), pp. 1-9, 2006.

[12] A. Cousin, O. Forni, S. Maurice, O. Gasnault, C. Fabre, V. Sautter, R.C. Wiens, J. Mazoyer, "Laser induced breakdown spectroscopy library for the Martian environment," Spectrochim. Acta B. Vol. 66, pp. 805-814, 2011.

[13] http://www.nasa.gov/mission_pages/msl/multimedia/pia16819.html

[14] http://www.nasa.gov/mission_pages/msl/multimedia/pia16910.html

[15] S.J. Choi, J.J. Yoh, "Effective LIBS detection using double pulse at optimum configuration," Applied Spectroscopy, Vol. 65, 8, pp. 952-956, 2011.

[16] J. Gonzalez, C. Liu, J. Yoo, X. Mao, and R. E. Russo, "Double-pulse laser ablation inductively coupled plasma mass spectrometry,"

Spectrochimica Acta Part B Vol. 60, 1, pp. 27-31, 2005.

[17] X. Mao, X. Zeng, S.B. Wen, and R.E. Russo, “Time-resolved plasma properties for double pulsed laser-induced breakdown spectroscopy of silicon,” Spectrochimica Acta Part B Vol. 60, 7, pp. 960-967, 2005.

[18] V.I. Babushok, F.C. DeLucia, J.L. Gottfried, C.A. Munson, and A.W. Miziolek, “Double pulse laser ablation and plasma: Laser induced breakdown spectroscopy signal enhancement,” Spectrochimica Acta Part B, Vol. 61, 9, pp. 999-1014, 2006.

[19] J.L. Gottfried, F.C. DeLucia, C.A. Munson, and A.W. Miziolek, “Standoff Detection of Chemical and Biological Threats Using Laser-Induced Breakdown Spectroscopy,” Applied Spectroscopy, Vol. 62, 4, pp. 353-363, 2008.

[20] V. Bulatov, L. Xu, I. Schechter, “Spectroscopic Imaging of Laser-Induced Plasma,” Analytical Chemistry, Vol. 68, 17, pp. 2966-2973, 1996.

[21] S. Darwiche, M. Benmansour, N. Eliezer, D. Morvan, “Investigation of optimized experimental parameters including laser wavelength for boron measurement in photovoltaic grade silicon using laser-induced breakdown spectroscopy,” Spectrochimica Acta Part B, Vol. 65, pp. 738-743, 2010.

[22] S.J. Choi, K.J. Lee, J.J. Yoh, “Quantitative laser-induced breakdown spectroscopy of standard reference materials of various categories,” Applied Physics B, Vol. 113, 3, pp. 379-388, 2013.

[23] L.C. Trevizan, D. Santos Jr, R.E. Samad, N.D. Vieira Jr, C.S. Nomura, L.C. Nunes, I.A. Rufini, F.J. Krug, “Evaluation of laser induced breakdown spectroscopy for the determination of micronutrients in plant materials,” Spectrochimica Acta Part B, Vol. 64, 5, pp. 369–377, 2009.

[24] J.W. Batista Braga, L.C. Trevizan, L.C. Nunes, I.A. Rufinib, D. Santos Jr, F.J. Krug, “Comparison of univariate and multivariate calibration for the determination of micronutrients in pellets of plant materials by laser induced breakdown spectrometry,” Spectrochimica Acta Part B Vol. 65, 1,

pp. 66–74, 2010.

[25] A.M. Popov, F. Colao, R. Fantoni, “Spatial confinement of laser induced plasma to enhance LIBS sensitivity for trace elements determination in soils,” J. Anal. At. Spectrom., Vol. 25, pp. 837–848, 2010.

[26] M.F. Alberghina, R. Barraco, M. Brai, T. Schillaci, L. Tranchina, “Comparison of LIBS and μ-XRF measurements on bronze alloys for monitoring plasma effects,” J. Phys. Conf. Ser. Vol. 275, pp. 1-11, 2011.

[27] D. DI´az, D.W. Hahn, A. Molina, “Evaluation of Laser-Induced Breakdown spectroscopy (LIBS) as a Measurement Technique for Evaluation of Total Elemental Concentration in Soils,” Appl Spectros, Vol. 66, pp. 99-106, 2012.

[28] K.K. Ayyalasomayajula, D.L. McIntyre, J. Jain, J.P. Singh, F. Yu-Yueh, “Determination of elemental impurities in plastic calibration standards using laser-induced breakdown spectroscopy,” Appl. Opt. Vol. 51, 7, pp. B143–B148, 2012.

[29] J.L. Tarazona, J. Guerrero, R. Cabanzo, E. Mejı´a-Ospino, “Construction of a predictive model for concentration of nickel and vanadium in vacuum residues of crude oils using artificial neural networks and LIBS,” Appl. Optics Vol. 51, 7, pp. B108–B114, 2012.

[30] P. Sobron, A. Wang, F. Sobron, “Extraction of compositional and hydration information of sulfates from laser induced plasma spectra recorded under Mars atmospheric conditions - Implications for ChemCam investigations on Curiosity rover,” Spectrochimica Acta Part B, Vol. 68, pp. 1–16, 2012.

[31] S.I. Gornushkin, I.B. Gornushkin, J.M. Anzano, B.W. Smith, J.D. Winefordner, “Effective normalization technique for correction of matrix effects in laser-induced breakdown spectroscopy detection of magnesium in powdered samples,” Appl. Spectrosc., Vol. 56, pp. 433-436, 2002.

[32] J.S. Huang, C.B. Ke, K.C. Lin, “Matrix effect on emission, current

correlated analysis in laser-induced breakdown spectroscopy of liquid droplets," Spectrochimica Acta Part B, Vol. 59, pp. 321-326, 2004.

[33] J.R. Dettman, J.W. Olesik, "Reduction of matrix effects in quantitative and semi-quantitative inductively coupled plasma-optical emission spectrometry using a partial local thermodynamic equilibrium model and an internal standard," Spectrochimica Acta Part B, Vol. 76, pp. 96-108, 2012.

[34] D. Bulajic, M. Corsi, G. Cristoforetti, S. Legnaioli, V. Palleschi, A. Salvetti, E. Tognoni, "A procedure for correcting self-absorption in calibration free-laser induced breakdown spectroscopy," Spectrochimica Acta Part B, Vol. 57, pp. 339-353, 2002.

[35] J. Zhang, G. Ma, H. Zhu, J. Xi, Z. Ji, "Accurate quantitative analysis of metal oxides by laser-induced breakdown spectroscopy with a fixed plasma temperature calibration method," J. Anal. At. Spectrom., Vol. 27, pp. 1903–1908, 2012.

[36] R.B. Anderson, J.F. Bell, R.C. Wiens, R.V. Morris, S.M. Clegg, "Clustering and training set selection methods for improving the accuracy of quantitative laser induced breakdown spectroscopy," Spectrochimica Acta Part B, Vol. 70, pp. 24-32, 2012.

[37] F.R. Doucet, T.F. Belliveau, J-l Fortier, J. Hubert, "Use of chemometrics and laser-induced breakdown spectroscopy for quantitative analysis of major and minor elements in aluminum alloys," Appl. Spectrosc., Vol. 61, 3, pp. 327-332, 2007.

[38] F.R. Doucet, P.J. Faustino, M. Sabsabi, R.C. Lyon, "Quantitative molecular analysis with molecular bands emission using laser induced breakdown spectroscopy and chemometrics," J. Anal. At. Spectrom., Vol. 23, pp. 694–701, 2008.

[39] https://www-s.nist.gov/srmors/

[40] S.J. Choi, J.J. Yoh, "Laser-induced plasma peculiarity at low pressures

from the elemental lifetime perspective," Opt. Express, Vol. 19, 23, pp. 23097-23103, 2011.

[41] A.J. Effenberger, Jr., J.R. Scott, “Effect of atmospheric conditions on LIBS spectra,” Sensors, Vol. 10, pp. 4907-4925, 2010.

[42] J.S. Cowpe, R.D. Pilkington, “Swagelok Ultra-Torr based feed-through design for coupling optical fibre bundles into vacuum systems”, Vacuum, Vol. 82, pp. 1341-1343, 2008.

[43] http://www.nist.gov/pml/data/asd.cfm

[44] S. Yalcin, Y.Y. Tsui, R. Fedosejevs, “Pressure dependence of emission intensity in femtosecond laser-induced breakdown spectroscopy,” J. Anal. Atomic Spectrom, Vol. 19, pp. 1295-1301, 2004.

[45] A.W. Miziolek, V. Palleschi, I. Schechter, “Laser-induced breakdown spectroscopy (LIBS): fundamentals and applications,” Cambridge University Press, 2006.

[46] C.B. Dreyer, G.S. Mungas, P. Thanh, J. G. Radziszewski, “Study of sub-mJ-excited laser-induced plasma combined with Raman spectroscopy under Mars atmosphere-simulated conditions,” Spectrochimica Acta Part B, Vol. 62, pp. 1448-1459, 2007.

[47] J.S. Cowpe, R.D. Pilkington, J.S. Astin, A.E. Hill, “The effect of ambient pressure on laser-induced silicon plasma temperature, density and morphology,” J. Phys. D: Appl. Phys., Vol. 42, pp. 165202, 2009.

[48] S.S. Harilal, C.V. Bindhu, V.P.N. Nampoori, C.P.G. Vallabhan, “Influence of ambient gas on the temperature and density of laser produced carbon plasma,” Appl. Phys. Lett., Vol. 72, 1998.

[49] K. Denbigh, “The principles of chemical equilibrium,” Cambridge University Press, 1968.

[50] http://www.ptable.com/?lang=en

[51] K.J. Lee, S.J. Choi, J.J. Yoh, “Stand-off laser-induced breakdown spectroscopy of aluminum and geochemical reference materials at

pressure below 1 torr," Spectrochimica Acta Part B, Vol. 101, pp. 335-341, 2014.

[52] S. Palanco, C. Lopez-Moreno, J.J. Laserna, Design, construction and assessment of a field-deployable laser-induced breakdown spectrometer for remote elemental sensing, Spectrochim. Acta B. Vol. 61, pp. 88-95, 2006.

[53] L.A. Alvarez-Trujillo, A. Ferrero, J.J. Laserna, Preliminary studies on stand-off laser induced breakdown spectroscopy detection of aerosols, J. Anal. At. Spectrom. Vol. 23, pp. 885-888, 2008.

[54] J.J. Laserna, R.F. Reyes, R. Gonzalez, L. Tobaria, P. Lucena, Study on the effect of beam propagation through atmospheric turbulence on standoff nanosecond laser induced breakdown spectroscopy measurements, Opt. Express. Vol. 17(12), pp. 10265-10276, 2009.

[55] P. Lucena, I. Gaona, J. Moros, J.J. Laserna, Location and detection of explosive-contaminated human fingerprints on distant targets using standoff laser-induced breakdown spectroscopy, Spectrochim. Acta B. Vol. 85, pp. 71-77, 2013.

[56] J.L. Gottfried, F.C. De Lucia Jr., C.A. Munson, A.W. Miziolek, Double-pulse standoff laser-induced breakdown spectroscopy for versatile hazardous materials detection, Spectrochim. Acta B. Vol. 62, pp. 1405-1411, 2007.

[57] J.L. Gottfried, R.S. Harmon, F.C. De Lucia Jr., A.W. Miziolek, Multivariate analysis of laser-induced breakdown spectroscopy chemical signatures for geomaterial classification, Spectrochim. Acta Part B. Vol. 64, pp. 1009-1019, 2009.

[58] F.C. De Lucia Jr., J.L. Gottfried, Classification of explosive residues on organic substrates using laser induced breakdown spectroscopy, Appl. Opt. Vol. 51(7), pp. B83-B92, 2012.

[59] J.L. Gottfried, Influence of metal substrates on the detection of explosive

residues with laser-induced breakdown spectroscopy, Appl. Opt. Vol. 52(4), pp. B10-B19, 2013.

[60] S.J. Choi, K.J. Lee, J.J. Yoh, “The laser-induced plasma persistence time extension in low pressures using the ablated mass confinement method,” Spectrochimica Acta Part B, Vol. 97, pp. 113-117, 2014.

[61] S.J. Choi, J.J. Choi, J.J. Yoh, “Novel control of plasma expansion direction aimed at very low pressure laser-induced plasma spectroscopy,” Optics Express, in review, 2014.

[62] J.R. Freeman, S.S. Harilal, P.K. Diwakar, B. Verhoff, A. Hassanein, “Comparison of optical emission from nanosecond and femtosecond laser produced plasma in atmosphere and vacuum conditions,” Spectrochimica Acta Part B, Vol. 87, 5, pp. 43-50, 2013.

[63] X. K. Shen, J. Sun, H. Ling, and Y. F. Lu, “Spectroscopic study of laser-induced Al plasmas with cylindrical confinement,” J. Appl. Phys., Vol. 102, 9, pp. 093301, 2007.

[64] L. B. Guo, Z.Q. Hao, M. Shen, W. Xiong, X. N. He, Z.Q.Xie, M. Gao, X.Y. Li, X. Y. Zeng, and Y. F. Lu, “Accuracy improvement of quantitative analysis by spatial confinement in laser-induced breakdown spectroscopy,” Opt. Express, Vol. 21, 15, pp. 18188-18195, 2013.

[65] L. B. Guo, B. Y. Zhang, X. N. He, C. M. Li, Y. S. Zhou, T. Wu, J. B. Park, X. Y. Zeng, and Y. F. Lu, “Optimally enhanced optical emission in laser-induced breakdown spectroscopy by combining spatial confinement and dual-pulse irradiation,” Opt. Express, Vol. 20, 2, pp. 1436-1443, 2012.

[66] A.M. Popov, F. Colao, and R. Fantoni, “Spatial confinement of laser-induced plasma to enhance LIBS sensitivity for trace elements determination in soils,” J. Anal. At. Spectrom. Vol. 25(6), pp. 837-848, 2010.

[67] D. Ding, P. Liang, J. Wu, N. Xu, Z. Ying, and J. Sun, “A comparative study of the enhancement of molecular emission in a spatially confined

plume through optical emission spectroscopy and probe beam deflection measurements," Spectrochimica Acta Part B, Vol. 79-80, pp. 44-50, 2013.

[68] S. Tao, and B. Wu, "Nanosecond laser pulse interactions with breakdown plasma in gas medium confined in a microhole," Appl. Phys. B, 2013.

[69] X. Zeng, X. Mao, S.S. Mao, S. Wen, R. Greif, and R.E. Russo, "Laser-induced shockwave propagation from ablation in a cavity," Appl. Phys. Lett., Vol. 88, pp. 061502, 2006.

[70] S.S. Mao, X. Zeng, X. Mao and R.E. Russo, "Laser-induced breakdown spectroscopy: flat surface vs. cavity structures," J. Anal. At. Spectrom., Vol. 19, pp. 495-498, 2004.

[71] Z. Hou, Z. Wang, J. Liu, W. Ni, Z. Li, "Combination of cylindrical confinement and spark discharge for signal improvement using laser induced breakdown spectroscopy," Opt. Express, Vol. 22, 11, pp. 12909-12914, 2014.

[72] M. Corsi, G. Cristoforetti, M. Hidalgo, D. Iriarte, S. Legnaioli, V. Palleschi, A. Salvetti, and E. Tognoni, "Effect of laser-induced crater depth in laser-induced breakdown spectroscopy emission features," Appl. Spectrosc., Vol. 59, 7, pp. 853–860, 2005.

[73] Z. Hao, L. Guo, C. Li, M. Shen, X. Zou, X. Li, Y. Lu, X. Zeng, "Sensitivity improvement in the detection of V and Mn elements in steel using laser-induced breakdown spectroscopy with ring-magnet confinement," J. Anal. At. Spectrom., DOI: 10.1039/c4ja00144c, 2014.

[74] C. Li, J. Wang, X. Wang, "Shock wave confinement-induced plume temperature increase in laser-induced breakdown spectroscopy," Physics Letter A, Vol. 378, 45, pp. 3319–3325, 2014.

[75] V.S. Burakov, N.V. Tarasenko, M.I. Nedelko, V.A. Kononov, N.N. Vasilev, S.N. Isakov, "Analysis of lead and sulfur in environmental samples by double pulse laser induced breakdown spectroscopy," Spectrochimica Acta Part B, Vol. 64, 2, pp. 141-146, 2009.

[76] F. Weritz, S. Ryahi, D. Schaurich, A. Taffe, G. Wilsch, “Quantitative determination of sulfur content in concrete with laser-induced breakdown spectroscopy,” Spectrochimica Acta Part B, Vol. 60, 7-8, pp. 1121-1131, 2005.

[77] G. Asimellis, S. Hamilton, A. Giannoudakos, M. Kompitsas, “Controlled inert gas environment for enhanced chlorine and fluorine detection in the visible and near-infrared by laser-induced breakdown spectroscopy,” Spectrochimica Acta Part B, Vol. 60, 7-8, pp. 1132-1139, 2005.

초 록

레이저 유도 플라즈마 분광분석법 (LIBS : Laser-Induced Breakdown Spectroscopy) 은 샘플에 레이저를 조사했을 때 발생하는 플라즈마를 활용한 실시간 비접촉 성분 분석 기법이다. 레이저 에너지를 집중시켜 10^9 W/cm^2 이상의 높은 에너지 밀도로 조사하면 샘플이 고온 고압의 플라즈마 형태로 붕괴된다. 플라즈마는 이온, 원자, 전자, 분자 등이 공존하는 상태로, 여기된 물질이 에너지를 잃고 안정한 상태로 되돌아 가면서 원소의 성분과 여기 상태에 따라 특정한 파장의 빛을 방출한다. 이때 방출된 빛의 파장을 분석하여 물질의 구성 성분을 정성 · 정량적으로 분석할 수 있다.

LIBS는 실시간으로 물질의 성분 분석이 가능하고, 샘플의 전처리 과정 없이 비접촉으로 검출할 수 있는 기법이라는 점에서 우주 탐사 착륙선의 로버에 탑재되어 탐사 임무를 수행할 수 있다. 본 연구에서는 LIBS 기술의 우주 활용을 위한 기초 연구를 수행하였다.

실제 우주 탐사에 LIBS 기술을 적용하고 있는 NASA의 정보를 바탕으로 우주 탐사 탑재체에 요구되는 LIBS 규격을 규명하고, 우주 환경을 모사하는 진공 챔버를 구축함으로써 실제 운용 환경을 고려한 연구의 기반을 마련하였다. 레이저와 시편의 특성에 대한 신호 영향을 파악하고, 이를 낮은 압력 조건에 적용하여 변화하는 운용 환경에서도 특성의 예측이 가능하도록 데이터 베이스를 구축하였다. 위의 결과는 시스템 운용 조건과 그에 대한 결과를 물리화학적인 관점에서 분석함으로써 LIBS 연구 분야에 현재까지 알려져 있지 않았던 결론을 도출하였다.

탐사 대상 물질의 농도 분석을 위하여 우주 탐사에 적합한 표준

물질을 활용하여 압력, 원소, 시편의 특성에 대한 검량선을 작성하고 특성을 규명함으로써 정량 분석 데이터 베이스를 구축하였고 특성을 예측할 수 있도록 하였다. 특히 기존의 연구와 다르게 6가지의 그룹으로 분류된 다양한 표준 물질을 사용함으로써 정량 분석 시 가장 큰 문제가 되는 매트릭스 효과를 극복하여 정확도를 향상시켰다. 또한 단변량/다변량 기법에 의한 정량 분석을 통하여 검량선의 상관계수를 향상시킴으로써 매트릭스 효과에 의한 오차를 보정할 수 있었다.

실제 탐사를 위하여 5~7 m 원거리 검출 연구가 수행되었으며, 최종적으로 소형화된 LIBS 장비를 제작하여 소형화 장비의 성능을 검증하고 탑재체로써의 LIBS 시스템 활용 가능성을 확인하였다.

실제 탐사 환경에 해당하는 저압 조건에서는 플라즈마가 급격히 팽창하여 소멸하는 문제가 있다. 이러한 문제점을 해결하고 저압에서의 검출 성능을 향상시키기 위하여 플라즈마의 팽창을 물리적으로 막고 팽창 방향을 제어하기 위한 confinement 기법 연구가 수행되었다. 기존에는 0.1 torr 이하의 압력 환경에서는 ICCD 검출기를 사용해야 플라즈마 검출이 가능하였는데, confinement 기법을 도입함으로써 CCD 검출기를 활용한 저압 검출이 가능하였다. 또한 신호세기가 크게 향상되었고, 낮은 에너지로도 검출이 가능하게 됨으로써 전체 시스템의 소형화 가능성을 확인하였다.

LIBS의 응용 범위로는 바이오 연료 개발 과정에서 중간 공정 장비의 손상을 야기하는 염소와 황의 검출 방법이 주목받고 있는 가운데 LIBS를 바이오 연료 개발에 접목할 수 있다. 녹색 산업의 중요성이 대두되면서 그동안 안정성을 중요시하여 규제하지 않았던 항공 매연의 규제가 이루어질 시기이므로 항공 매연의 실시간 검출에 응용되어 매연 규제 및 환경 오염 방지를 가능하게 한다. 또한 고에

너지 위험 물질 검출. 독성 물질 분석을 통한 제어 · 관리 및 대기 중 중금속 입자의 실시간 분석, 그리고 치아, 석회화 조직, 인체 피부, 인체 모발, 박테리아 연구에 이르기까지 다양한 생체 공학 연구에 LIBS 성분 분석법이 응용되고 있다. 또한 범죄수사학적인 측면에서 지문 분석에도 적용이 가능하다.

본 연구를 통하여 LIBS 시스템을 탐사 탑재체로 활용할 수 있는 가능성을 다각도로 검증하였다. 또한 위에서 언급한 다양한 활용 분야에 있어서 본 연구의 결과는 목적에 적합한 시스템 설계를 위한 일련의 참고 자료가 될 수 있다.

주요어: 레이저 유도 플라즈마 분광분석법, 플라즈마, 레이저 삭마, 우주 탐사, 저압 환경, 성분 분석

학 번: 2008-20799